ISSN 0915-6364

NATIONAL INSTITUTE FOR FUSION SCIENCE

Effect of Recombination Processes on FeXXIII Line Intensities

I. Murakami, K. Moribayashi and T. Kato

(Received - Feb. 5, 1998)

NIFS-DATA-47 May 1998

RESEARCH REPORT
NIFS-DATA Series

NAGOYA, JAPAN

Effect of Recombination Processes on FeXXIII Line Intensities

Izumi Murakami, Kengo Moribayashi*, and Takako Kato
National Institute for Fusion Science, Toki, Gifu 509-5292, Japan

Abstract

We have constructed a collisional-radiative model for Be-like Fe ion (Fe^{22+}) to calculate the intensities of FeXXIII spectral lines in non equilibrium ionization plasma. In the model we consider levels with $n \lesssim 70$ and take into account the ionization and recombination processes to/from Fe^{23+} ion. The recombining processes of Fe^{22+} ion had not been considered in detail in models for the spectral lines. We calculate the dielectronic recombination rate coefficients into the excited states with use of the Cowan's code. We examine the effect of radiative cascades from levels with $n \gtrsim 5$ to the population densities and find it is important especially for the recombining plasma. We study the line intensities and the intensity ratios as a function of an electron temperature at an electron density of $10^{14}cm^{-3}$ for a plasma in non equilibrium ionization with arbitrary ion abundance ratio of Fe^{23+} ion to Fe^{22+} ion. The dielectronic satellite lines and the radiative loss by Fe^{22+} ion are also discussed.

Keywords: FeXXIII, dielectronic recombination rate coefficient, non-equilibrium ionization plasma, population densities, spectral line intensities, intensity ratios, plasma diagnostics

*current address: Advanced Photon Research Center, Kansai Research Establish, Japan Atomic Energy Research Institute, 25-1, Mii-minami-cho, Neyagawa-shi, 572, Japan

1 Introduction

Iron atom and ions exist as impurities in laboratory, fusion, and astrophysical plasmas. Such impurities play important rolls in plasmas as coolant or as a tool to know condition of plasmas. Intensity ratios of spectral lines of ions can be used for plasma diagnostics. In a plasma at an electron temperature of $\sim$ 1keV, such as in laboratory plasmas [1], [2], [3], [4], solar flares [5], [6], [7], or hot gas in elliptical galaxies [8] and clusters of galaxies [9], iron exists as Fe^{22+} (Be-like Fe) or Fe^{23+} (Li-like Fe) ions. The study of FeXXIII spectral lines provides us the information of these plasmas. Especially in astrophysical plasmas, iron is important to be observed in order to measure the heavy element abundance. Recently the observations of elliptical galaxies and clusters of galaxies by the X-ray satellite *ASCA* in the 0.7-2keV spectral band show discrepancies with model predictions by standard plasma emission codes of [10] and [11]. Liedhal, Osterheld, and Goldstein (1995) [12] presented new calculations using the HULLAC code including levels of principal quantum number, $n \leq 7$. In the code all transition rate coefficients were calculated. Their calculations show better agreement with observations than previous models but still disagreement remains. Savin et al.(1996) [4] carried out laboratory measurements of FeXXIV line emissions using the Lawrence Livermore electron beam ion trap to examine the issue. The measured emission line ratios of $(n = 4 \rightarrow 2)$ and $(n = 3 \rightarrow 2)$ transitions are found in good agreement with theoretical calculations by distorted wave code of Zhang, Sampson, and Clark (1990) [13] within $1 \sim 1.1\sigma$ and by the HULLAC code [12] within $1 \sim 1.3\sigma$. The FeXXIII emission lines still remain to be examined experimentally and theoretically.

We have studied FeXXIII spectral lines and their possibility of the electron temperature diagnostics. We have constructed a Collisional-Radiative Model (CRM) for Fe^{22+} ion to calculate the population densities of the excited states and the emission line intensities. This model takes into account collisional excitation/de-excitation and radiative transitions, and the ionization and recombination to/from the Li-like Fe ion. Previously we started the CRM, considering 98 levels of $2s^2$, 2s2p, $2p^2$, $2snl$, and $2pnl$ states with the principal quantum number n up to 4 (Murakami, Kato, & Dubau 1996, Paper I; Murakami & Kato 1996, Paper II). This model did not include the ionization and recombination processes and the level population densities are mainly excited from the ground state of Fe^{22+} ion.

In an ionization equilibrium plasma of $T_e \sim$ 1keV relative abundance of Fe^{23+} to Fe^{22+} ions is close to unity and recombination processes from Fe^{23+} ion should be considered when examining population densities of Fe^{22+} ion. In this work we extend the model including much more levels than Paper II of $2snl$ states up to $n = 70$ and $2pnl$ states up to $n = 10$ in order to consider the recombination processes, since radiative cascades play an important roll, especially for the recombining plasma. Liedhal et al. took into account the recombination processes in their HULLAC code, but they focused on the bulk ratio of $(4 \rightarrow 2)$ and $(3 \rightarrow 2)$ transitions and did not examine the details of each line. Kallman et al. [14] presented calculations of the emission spectra from photo-ionized gases for all L-shell Fe ions, considering levels of $n \leq 4$. In the photo-ionized plasma the recombination processes, such as dielectronic recombination, radiative recombination, and three body recombination, dominate the population densities of excited states. They adopted the dielectronic recombination and collisional ionization rates of Arnaud and Raymond (1992) [15] who only gave the total rates. It is unclear how they estimated the dielectronic recombination rate coefficient of each state, so their results seem to have ambiguities. In our model we have adopted the dielectronic recombination rate coefficient for each level calculated with the Cowan's code. With this model we calculate the emission line inten-

sities for a ionization equilibrium plasma and a non-equilibrium ionization plasma with arbitrary ion density ratio of Fe^{23+} ion to Fe^{22+} ion. We examine the electron temperature dependences of the line intensity ratios and consider the temperature diagnostics.

In §2 we describe our CRM. Atomic data for the CRM are shown in §3. The results for the population densities of the excited states, the line intensities, and the intensity ratios are discussed in §4. We obtain the radiative power loss, the effective ionization rate, and the effective recombination rate in §5.

2 Collisional-Radiative Model

The population densities of excited states are calculated by the CRM. We assume the quasi-steady state for excited states and solve the rate equations including all transitions between excited states. The rate equation for the population density of level i, n_i, is

$$\begin{aligned}\frac{dn(i)}{dt} &= -\sum_{j\neq i}[C(i,j)n_e + A_r(i,j)]n(i) + \sum_{j\neq i} C(j,i)n_e n(j) + \sum_{j>i} A_r(j,i)n(i) \\ &\quad -S(i)n(i)n_e + [\alpha_d(i) + \alpha_r(i) + \alpha_t(i)n_e]n_e n(\mathrm{Fe}^{23+}) \\ &= 0 \quad for\ i > 1, \end{aligned} \tag{1}$$

where $C(i,j)$ is the collisional excitation / deexcitation rate coefficients from the level i to j, $A_r(i,j)$ is the radiative transition probability from i to j, n_e is the electron density, $n(\mathrm{Fe}^{23+})$ is the density of Fe^{23+} ground state $1s^22s$, $S(i)$ is the ionization rate coefficients from the level i, $\alpha_d(i)$ is the dielectronic recombination rate coefficient, $\alpha_r(i)$ is the radiative recombination rate coefficient, and $\alpha_t(i)$ is the three-body recombination rate coefficient to the level i, from the ground state of Fe^{23+} ions.

The population densities are solved as a combination of two parts; one is proportional to the density of the ground state of Fe^{22+} , and the other is proportional to the density of the ground state of Fe^{23+} . We call the former part an ionizing plasma component and the latter a recombining plasma component. The rate equations can be solved separately as a pure ionizing plasma which is governed with the collisional excitation from the ground state and does not include the recombination processes, and as a pure recombining plasma which is governed with the recombination processes and does not include the collisional excitation from the ground state:

$$n(i) = N_I(i)n_1 + N_R(i)n(\mathrm{Fe}^{23+}), \tag{2}$$

$$\begin{aligned}\frac{dN_I(i)}{dt} &= -\sum_{j\neq i}[C(i,j)n_e + A_r(i,j)]N_I(i) + \sum_{j\neq i,1} C(j,i)n_e N_I(j) + \sum_{j>i} A_r(j,i)N_I(j) \\ &\quad -S(i)N_I(i)n_e + C(1,i)n_e \\ &= 0, \end{aligned} \tag{3}$$

$$\begin{aligned}\frac{dN_R(i)}{dt} &= -\sum_{j\neq i}[C(i,j)n_e + A_r(i,j)]N_R(i) + \sum_{j\neq i,1} C(j,i)n_e N_R(j) + \sum_{j>i} A_r(j,i)N_R(j) \\ &\quad -S(i)N_R(i)n_e + [\alpha_d(i) + \alpha_r(i) + \alpha_t(i)n_e]n_e \\ &= 0. \end{aligned} \tag{4}$$

We can then obtain the population densities of the excited states for a plasma in ionization equilibrium or for a non equilibrium ionization plasma assuming any density ratio of the Fe^{23+} ground state to Fe^{22+} ground state, $n(Fe^{23+})/n_1$.

We define the effective emission rate coefficients, which is the emission line intensity per electron and per ion, for ionizing plasma component and recombining plasma component as follows:

$$C_I^{eff}(i,j) = A_r(i,j)N_I(i)/n_e, \quad (5)$$
$$C_R^{eff}(i,j) = A_r(i,j)N_R(i)/n_e. \quad (6)$$

3 Atomic Data

3.1 Energy Levels and Transition Probabilities

All 98 fine structure levels of $1s^2 2snl\ ^{2S+1}L_J$ and $1s^2 2pnl\ ^{2S+1}L_J$ states with $n \leq 4$ are considered. For $5 \leq n \leq 10$ levels, we considered $1s^2 2snl\ ^{2S+1}L$ and $1s^2 2pnl\ ^{2S+1}L$ configurations (328 levels). We treat $1s^2 2snl$ states bundling together with different l levels for $n = 11 - 70$, since the energy difference between different l levels with the same n becomes quite small for large n levels. Above a critical levels with the principal quantum number n_c the population densities of the excited states are governed by the collision processes and the levels are in the local thermodynamic equilibrium. The critical quantum number n_c is estimated with hydrogenic approximation as

$$n_c \approx \left[\frac{7 \times 10^{17}\mathrm{cm}^{-3}}{\mathrm{n_e}}\left(\frac{kT_e}{Z_{eff}^2 I_H}\right)^{1/2} Z_{eff}^7\right]^{2/17}, \quad (7)$$

where I_H is the ionization potential of Hydrogen and Z_{eff} is the effective charge and $Z_{eff} = Z - 3$ for Be-like ions where Z is the nuclear charge. The critical quantum number then becomes about 76 at $n_e = 10^{11}\mathrm{cm}^{-3}$ and $T_e = 1\mathrm{keV}$, or 34 at $n_e = 10^{14}\mathrm{cm}^{-3}$ and $T_e = 1\mathrm{keV}$. For the former case the levels included in the CRM is slightly incomplete but the effect to the population densities is negligible. The $1s^2 2pnl$ states with $n \geq 11$ are autoionizing states; above the ionizing threshold, $1s^2 2s$. We do not include the autoionizing states in the CRM.

Energy levels and transition probabilities of $n \leq 4$ states are calculated by SUPERSTRUCTURE code of AUTOLSJ method (Paper I). For $5 \leq n \leq 10$ those are calculated with the Cowan's code. For $11 \leq n \leq 70$, energy levels under the ionization limit are calculated with screening theory (Safronova et al. [18]), and transition probabilities are calculated with hydrogenic approximation.

We have included a magnetic quadrupole transition probability for $2s^2\ ^1S_0 - 2s2p\ ^3P_2$ (Nussbaumer & Storey [19]), magnetic dipole transition probabilities for $2s2p(^3P_0 - {}^3P_1)$ and for $2s2p(^3P_1 - {}^3P_2)$ and an electric quadrupole transition probability for $2s2p(^3P_0 - {}^3P_2)$ (Bhatia and Mason [20]).

3.2 Collisional excitation Rate Coefficients

We have adopted data by Zhang & Sampson (1992) [21] for the $\Delta n = 0$ transitions with n=2, and data by Sampson, Goett, & Clark (1984) [22] for all fine-structure transitions between $n = 2$ and $n = 3$. We have used modified Mewe's empirical formula [23] for other transitions. The excitation rate coefficients calculated by Mewe's empirical formula are checked for available transitions with above data. Details on the modifications are described in Paper I. Two electron transitions between $n \geq 7$ levels such as 2s9l - 2p7l are ignored.

We have included the proton collisional excitation for the three fine-structure transitions in the 2s2p ^{3}P levels, using the cross section given by Doyle [24].

3.3 Recombination and Ionization Rate Coefficients

In this section we consider the recombination from Li-like ground state $1s^2 2s$ and the ionization to the Li-like ground state.

3.3.1 Dielectronic Recombination Rate Coefficients

The dielectronic recombination process from Li-like Fe ions to Be-like Fe ions,

$$\begin{aligned} \mathrm{Fe}^{23+}\ (1s^2 2s) + e^- &\rightarrow \mathrm{Fe}^{22+\,**}(1s^2 2pnl(n \geq 11), 1s^2 3l_1 n' l_2) \\ &\rightarrow \mathrm{Fe}^{22+\,*}(1s^2 2snl, 1s^2 2pn'l'(n \leq 10)) + h\nu, \end{aligned} \tag{8}$$

is examined. The energy levels, the autoionizing rate, A_a, and the radiative transition probabilities, $A_r(i,j)$, are calculated with use of the Cowan's code and we obtain the dielectronic recombination rate coefficients to the level j of $\mathrm{Fe}^{22+\,*}$ as

$$\alpha_d(i_0, j) = \frac{C(T_e)}{g_0} \sum_i Q_d(i,j) \exp\left(-\frac{E_s(i)}{kT_e}\right), \tag{9}$$

with

$$C(T_e) = \frac{1}{2}\left(\frac{h^2}{2\pi m k T_e}\right)^{3/2}, \tag{10}$$

$$Q_d(i,j) = \frac{g(i) A_a(i, i_0) A_r(i,j)}{\sum_{i'_0} A_a(i, i'_0) + \sum_k A_r(i,k)}, \tag{11}$$

where i_0 is the ground state of Fe^{23+} , i'_0 indicates excited and ground state of Fe^{23+} , g_0 and $g(i)$ are statistical weight of the ground state of Fe^{23+} and autoionizing state (i), $E_s(i)$ is the energy difference between the autoionizing state (i) and the ground state of Fe^{23+} ion (i_0), and T_e is the electron temperature. We calculate the dielectronic recombination rate coefficients for the levels with principal quantum number $n \leq 10$ by the Cowan's code. For the rate coefficients of 2snl levels with $n \geq 11$, we use the scaling formulae for A_a and A_r to estimate the recombination rate coefficients. The transitions through the autoionizing states of 2pnl and 3pnl are only considered when scaling formulae are used. Other transitions through $3l_1 nl_2$ $(l_1 \neq p)$ state can be neglected. For the transition through 3pnl states A_r and A_a can be scaled with using the values at $n = 7$:

$$A_r(3pnl \rightarrow 2snl) \simeq A_r(3p7l \rightarrow 2s7l), \tag{12}$$

$$A_a(3pnl \rightarrow i_0) \simeq A_a(3p7l \rightarrow i_0)(7/n)^3, \quad (13)$$

and then the dielectronic recombination rate coefficient is

$$\alpha_d(i_0, 2snl) \simeq \frac{C(T_e)}{g_0} \frac{g(i) A_a(3p7l, i_0)(7/n)^3 A_r(3p7l, 2s7l)}{\sum_{i_0'} A_a(3p7l, i_0')(7/n)^3 + \sum_k A_r(3p7l, k)} \exp\left(-\frac{E_s(3pnl)}{kT_e}\right). \quad (14)$$

For transition through 2pnl states, A_r and A_a are scaled with using values at $n = 11$, similarly to 3pnl.

Figure 1 shows the n dependence of the recombination rate coefficients. The rate coefficients to 2pnl levels are larger than those to 2snl. The rate coefficients to $n \geq 11$ levels decrease nearly in proportional to n^{-3} because of the scaling law assumed above.

The dielectronic recombination process emit satellite lines as the radiative transitions from the autoionizing states to the bound states. The line intensity of the satellite lines can be calculated as,

$$\begin{aligned} C_S^{eff}(i,j) &= I_S/(n_e n_1) \\ &= 3.3 \times 10^{-24} \left(\frac{I_H}{kT_e}\right)^{3/2} \left(\frac{Q_d(i,j)}{g_0}\right) e^{-\frac{E_s}{kT_e}} \left(\frac{n(\mathrm{Fe}^{23+})}{n_1}\right) \text{photons s}^{-1}. \end{aligned} \quad (15)$$

3.3.2 Radiative Recombination Rate Coefficients

The radiative recombination rate coefficients are obtained from the photo-ionization cross section with use of the Milne Relation (e.g. Rybicki and Lightman 1979). The photo-ionization cross sections for 2snl states with $n \leq 4$ are calculated by Clark, Cowan, and Bobrowicz (1986). With their cross section, the rate coefficients are calculated as

$$\alpha_r(i) = 4\pi c \left(\frac{\epsilon_i^2}{2\pi m c^2 kT_e}\right)^{3/2} \frac{2g(i)}{g_e g_0} \exp(\chi_i) \int_1^\infty \sigma_i^{bf}(u) u^2 \exp(-\chi_i u) du, \quad (16)$$

where $\chi_i = \epsilon_i/kT_e$, $u = h\nu/\epsilon_i$, ϵ_i is the ionization potential of the level i, and $g_e = 2$ is the statistical weight of electron.

For 2snl states with $n \geq 5$, the radiative recombination rate coefficients are estimated with the photo-ionization cross sections of hydrogenic approximation assuming the Gaunt factor as unity.

$$\alpha_r(i) = 2.60 \times 10^{-14} \frac{2g(i)}{g_e g_0} \frac{Z^4}{n^5} \left(\frac{I_H}{kT_e}\right)^{3/2} \exp(\chi_i) E_1(\chi_i) \mathrm{cm}^3 \mathrm{s}^{-1}, \quad (17)$$

where n is the principal quantum number, Z is the effective charge, $E_1(x)$ is the exponential integral.

The radiative recombination rate coefficients from the ground state of Fe^{23+} ion to 2pnl levels is taken to be zero. In order to include the radiative recombination to 2pnl levels, we need the population density of 2p level of Fe^{23+} , which should be obtained with a Collisional-Radiative Model for Fe^{23+} ion. So, we do not include such recombination process.

In Fig. 1 we also plot the n dependence of α_r. The α_r and α_d to the 2snl states are comparable. However, because of no transition of α_r from the Li-like ground state 2s to the 2pnl states, total radiative recombination rate is smaller than the total dielectronic recombination rate.

3.3.3 Three Body Recombination Rate Coefficients and Ionization Rate Coefficients

The three body recombination process is the inverse process of ionization by electron impact.

$$\alpha_t(i) = \frac{g(i)}{2g_0}\left(\frac{h^2}{2\pi mkT_e}\right)^{3/2} S(i)\exp\left(\frac{\epsilon_i}{kT_e}\right), \tag{18}$$

where ϵ_i is the ionization potential of the level i as in §3.3.2. The ionization rate coefficient from the level i, $S(i)$, is estimated with the Lotz's formula (Lotz 1967).

$$S(i) = 6.6\times10^{7}\frac{a_i\xi_i}{T_e(eV)}\left\{\frac{1}{\chi_i}\int_{\chi_i}^{\infty}\frac{e^{-x}}{x}dx - \frac{b_i e^{c_i}}{\chi_i + c_i}\int_{\chi_i+c_i}^{\infty}\frac{e^{-y}}{y}dy\right\}\mathrm{cm^3s^{-1}}, \tag{19}$$

where $\chi_i = \epsilon_i/T_e(eV)$. The parameters for the excited states are set to $\xi_i = 1$, $a_i = 4.5\times10^{-14}$ cm^2(eV)^2, and $b_i = c_i = 0$.

In Fig. 2 the temperature dependences of the total recombination rate coefficients at low density limit, α_d, α_r, and $\alpha_t n_e$ are plotted for T_e =100eV-10keV. Here the total means

$$\alpha_d = \sum_j \alpha_d(i_0, j), \tag{20}$$

$$\alpha_r = \sum_j \alpha_r(j), \tag{21}$$

$$\alpha_t n_e = \sum_j \alpha_t(j) n_e, \tag{22}$$

where the level j is taken up to $1s^2 2snl$ with $n = 70$.

The three body recombination rate coefficient with eq.(18) should be multiplied with the electron density. In this work we mainly consider the electron density of $10^{11} - 10^{14}$ cm^{-3} and the $\alpha_t n_e$ is much smaller than $\alpha_d(i)$ and $\alpha_r(i)$ at the electron density. The three body recombination rate coefficient becomes dominant when $n_e \gtrsim 10^{17}$cm^{-3} at T_e = 1keV or when $n_e \gtrsim 10^{15}$cm^{-3} at T_e = 100eV. As mentioned in §3.1 population densities of higher n levels which satisfy $n > n_c$ (eq.[7]) are considered in the LTE. In order to take into account the effect of the collisional processes in LTE population densities, we define the effective recombination rate coefficient which is the actual recombination rate coefficient into the ground state as follows,

$$\alpha_{eff} = \sum_{j>1} n(j)(A_r(j,1) + C(j,1)n_e)/n_e + \alpha_r(1) + \alpha_d(1) + \alpha_t(1)n_e, \tag{23}$$

where index 1 means the ground state. The effective recombination rate coefficients with the results of the CRM in the density region of $10^{11} - 10^{14}$cm^{-3} give the same values as the total recombination rate coefficient,

$$\alpha_{tot} = \alpha_d + \alpha_r + \alpha_t n_e = \sum_j \{\alpha_d(i_0, j) + \alpha_r(j) + \alpha_t(j)n_e\}, \tag{24}$$

in Fig. 2. It is because the direct recombination to the levels higher than n_c is small as shown in Fig. 1. The density effect of the effective recombination rate coefficients is discussed in Ref.[27].

4 Results

4.1 Population Densities

4.1.1 Electron density dependences

Density dependences of the population densities of the ionizing plasma component, $N_I(i)$, are presented in Figs. 3 and 4. At $n_e \lesssim 10^{20}\mathrm{cm}^{-3}$ the effect of collisional ionization is small and the density dependences are the same as in Paper I. Metastable state, 2s2p $^3P_0$, has constant population density at $n_e \lesssim 10^{12}\mathrm{cm}^{-3}$ because the radiative decay rate to the ground state is zero. Population densities of the other levels increase in proportionally to the electron density in the low density region, $n_e \lesssim 10^{12}\mathrm{cm}^{-3}$. However in the region of $n_e > 10^{20}\mathrm{cm}^{-3}$, each $N_I(i)$ approachs a constant value whith is smaller than one in Paper I, because the ionization from the excited states was not included in Paper I. The collisional ionization becomes significant at $n_e \gtrsim 10^{21}\mathrm{cm}^{-3}$ at $T = 1\mathrm{keV}$. Comparing Figs. 3a to 3b, we find that the collisional ionization is not significant at $T = 100$ eV and there are no decrements of the population densities of ionizing plasma component at high density limit, which are seen for $N_I(i)$ of $n = 2$ levels at $T = 1\mathrm{keV}$.

The population densities of the recombining plasma component, $N_R(i)$, approach to be distributed with the Saha-Boltzmann distribution, $n_{SB}(i)$, at high density limit:

$$n_{SB}(i) = \frac{g(i)}{2g_0}\left(\frac{h^2}{2\pi mkT_e}\right)^{3/2} n(\mathrm{Fe}^{23+})n_e \exp\left(-\frac{\epsilon(i)}{kT_e}\right). \tag{25}$$

In Fig. 5, $N_R(i)/(n_e g(i))$ is plotted as a function of the electron density and it approaches to a constant value at higher electron density, as expected.

When the temperature becomes lower, the Saha-Boltzmann population density as seen in eq.(25) becomes higher. The difference due to the temperature is significantly seen for $n = 3$ and 4 levels when we compare Figs. 5bc with 5ef. At $T = 100\mathrm{eV}$ the recombining plasma component, $N_R(i)/g(i)n_e$, increases for $n_e \gtrsim 10^{20}\mathrm{cm}^{-3}$ and reaches constant value at $n_e \gtrsim 10^{24}\mathrm{cm}^{-3}$ as shown in Fig. 5ef.

At intermediate density region both population density components, N_I and N_R, are affected by the collisional excitation from the metastable states, 2s2p $^3P_0$, $^3P_2$ and collisional excitation/de-excitation to/from other excited states

4.1.2 The Effect of Radiative Cascades

In Paper I we found that radiative cascades from upper levels are important for the population densities especially at higher temperature. Such cascades are basically important for the population densities of recombining plasma component, since the population densities of higher n levels are populated much easier by recombination process than by excitation process. Here we examine about radiative cascades from $n \geq 5$ levels, comparing with results of the CRM with $n \leq 4$ and those of the CRM with $n \leq 70$. In Fig. 6 the ratio of the population density calculated with the CRM including $n \leq 70$ to that with the CRM including $n \leq 4$ for ionizing plasma component and for recombining plasma component separately is plotted for each level.

For the ionizing plasma component, the population densities of the metastable state, 2s2p ^{3}P, for example, are enhanced about 10 % - 18 % at $T_e = 1\mathrm{keV}$ and $n_e = 10^{14}\mathrm{cm}^{-3}$ through radiative cascades from higher levels. In general, the population densities of triplet levels are much more enhanced than those of the singlet levels, and the 2pnl levels

than the $2snl$ levels, as found in Paper I. The contribution of the cascades increases as T_e increases, which is similar to what we saw in Paper I for cascades from $n = 3 - 4$ levels onto $n = 2$ and 3 levels.

For the recombining plasma component, the enhancement of the population densities by radiative cascades from n=5-70 are more significant than the ionizing plasma component. The population densities of the metastable states are larger than the result of the CRM with $n = 2-4$ by factor 2. For the recombining plasma component the contribution of the cascades does not change so much with the electron temperature.

4.1.3 Contribution of Recombination Processes

In order to see the relative contribution of the recombination processes to the population densities, here we examine the ratio, $R(i) = N_R(i)/N_I(i)$, as a function of n.

$$n(i) = N_I(i)n_1\,(1 + R(i)n(\mathrm{Fe}^{23+})/n_1)\,. \tag{26}$$

We simply take an average for $R(i)$ with the same principal quantum number n and plot it in Fig. 7 for $T_e = 1$keV and $n_e = 10^{14}$ cm^{-3}. $R(i)$ increases with increasing n, especially for $2pnl$ levels. For $2snl$ singlet levels $R(i)$ is less than 0.1 in average. These mean that the recombination processes contribute much to the population densities of triplet levels and $2pnl$ levels.

When the electron temperature increases, $R(i)$ decrease generally, because $N_I(i)$ increases or decreases slowly with the electron temperature and $N_R(i)$ on the other hand decreases faster.

4.2 Line Intensities

Figure 8 shows the synthetic spectra for pure ionizing plasma of Fe^{22+} ion (only ionizing plasma component) (Figs.8a,b,c,d,j,k,q), pure recombining plasma (only recombining plasma component) (Figs.8e,f,g,l,m,n,r,s), and the dielectronic satellite lines from Fe^{23+} to Fe^{22+} (Fig.8h,i,o,p,t,u). Figs.8a, 8b, 8e, 8j, 8l, 8q,and 8r are spectra for a plasma at $n_e = 10^{14}$cm^{-3} and $T_e = 1$keV (1.16×10^7K). Figs.8c, 8f, 8k, and 8m are for a plasma at $n_e = 10^{11}$cm^{-3} and $T_e = 1$keV (1.16×10^7K). Figs.8d, 8g, 8n, and 8s are for a plasma at $n_e = 10^{14}$cm^{-3} and $T_e = 100$eV. Figs.8h, 8o, and 8t are the dielectronic satellite lines at $T_e = 1$keV and Figs.8i, 8p, and 8u at $T_e = 100$eV. The lines which are strong in ionizing plasma are different from those in recombining plasma. In Tables 1-3 strong lines either for ionizing plasma component or recombining plasma component are listed with their transitions, transition probabilities, A (s^{-1}), wavelengths, λ (Å), and effective emission rate coefficients for ionizing plasma component, $C_I^{eff}(i,j)$, and those for recombining plasma component, $C_R^{eff}(i,j)$, at $T_e = 1$keV and $n_e = 10^{14}$cm^{-3}. Table 1 is for wavelength regions of $\lambda = 100-300$Å (mainly $\Delta n = 2-2$ transitions), Table 2 for $10-13$ Å (mainly $\Delta n = 3-2$ transitions), and Table 3 for $6-10$Å ($\Delta n = n'-2$ transitions where $n' = 4-10$). These wavelength regions are corresponding to Figs.8a-i, Figs.8j-p, and Figs.8q-u, respectively. In the tables we also list wavelengths published already for comparison [28]. The accuracy of our wavelengths is order of a few percent. In this paper we are interested in line intensities, not in wavelengths, so we do not discuss the difference further. The spectra and effective emission rate coefficients can be compared directly if the ion abundances of Fe^{22+} and Fe^{23+} are equal. At $T_e = 1$keV and $n_e = 10^{14}$cm^{-3} the emission lines of the pure recombining plasma are 10 times or much weaker than those

of the pure ionizing plasma. If a plasma is in ionization equilibrium, the ion abundance ratio of Fe^{23+} to Fe^{22+} is 1.1 at $T_e = 1$keV [15].

The satellite lines from Fe^{23+} to Fe^{22+} calculated with eq.(14) (Figs.8h,i,o,p,t,u) are factor 5 or much weaker than the spectral lines of the pure recombining plasma (Fig.8e, g, l, n, r, s). This result is quite different from the previously estimated intensities of satellite lines by empirical formula by Mewe, Gronenschild, and van den Oord (1985) [11]. Their model gives the Be-like iron satellite line intensities which have about 30% of the emission lines produced by direct excitation at $T_e = 1$keV.

In Paper I we chose 17 strong lines in an ionizing plasma and studied the electron density and electron temperature dependences of these lines and of the 14 line ratios. But here we select some more different lines for $n = 2 - 3$ transitions which are not contaminated with Fe^{23+} lines. (For FeXXIV lines, see Shirai et al. 1990 [28], for example.) We show the effective emission rate coefficients (eq.[5]) of selected lines as a function of the electron temperature in Fig. 9 for $n_e = 10^{14}\text{cm}^{-3}$ and $n_e = 10^{11}\text{cm}^{-3}$.

At $n_e = 10^{11} - 10^{14}\text{cm}^{-3}$, the population densities of $n \geq 3$ most levels and the line intensities emitted from such levels do not depend much on the electron density. Exceptions are transitions which upper levels have connections with 2s2p or $2p^2$ levels with the collitional excitation. As seen in §4.1, the population densities of 2s2p and $2p^2$ levels strongly depend on the electron density.

The effective emission rate coefficients of the ionizing plasma component of $n = 2 - 2$ transitions are decreasing functions of the electron temperature for $T_e \geq 100$eV, except for the transitions which upper levels are $2p^2$ levels, becuase the population densities of these levels are stronly enhanced by cascades from higher levels as we found in Paper I. On the other hand, the effective emission rate coefficients of the recombining plasma component are decreasing functions of the electron temparture and the recombination processes enhance the intensities at low temperature region when both components are comparable as seen in Fig. 9. In the figures the total effective emission rate coefficients in non-equilibrium ionization plasma with assmuing the ion abundance ratio of Fe^{23+} to Fe^{22+} ions or in the ionization equilibrium plasma, are plotted.

For $n = 3 - 2$ and $n = 4 - 2$ transitions the effective emission rate coefficients of ionizing plasma component are increasing functions of the electron temperature and have a peak at around a few keV, so the contribution of the recombining plasma component to the line intensities of the equilibrium plasma can be significant at low temperature region. The contributions of the recombining plasma components become important in non-equilibrium ionization plasma, or photo-ionized plasma heated by X-ray radiation at low electron temperature. At higher temperature region, contributions of the recombination plasma componet are small.

4.3 Line Intensity Ratios

The electron temperature and density dependence of the intensity ratios are useful for plasma diagnostics.

Figure 10 shows the temperature dependences of the intensity ratios of some line pairs for $n_e = 10^{14}\text{cm}^{-3}$ and for $n_e = 10^{11}\text{cm}^{-3}$. The spectral lines are indicated by $i - j$ of $C^{eff}(i,j)$, which is listed in Tables 1-3. In Fig.10 a solid line shows the intensity ratio for pure ionizing plasma (the ratio of ionizing plasma components only: $C_I^{eff}(i,j)/C_I^{eff}(k,l)$), and a dotted line shows the ratio for pure recombining plasma (recombining plasma components only: $C_R^{eff}(i,j)/C_R^{eff}(k,l)$). A dashed line shows the ratio

for ionization equilibrium plasma, and dot-dashed lines show the ratios of non-equilibrium ionizing plasma with given ion abundance ratio, r, of Fe^{23+} and Fe^{22+} from 0.1 to 300: $\{(C_I^{eff}(i,j) + C_R^{eff}(i,j) * r)/(C_I^{eff}(k,l) + C_R^{eff}(k,l) * r)\}$. The temperature dependences are not strong for most line intensity ratios. Some line ratios of the ionizing plasma components vary as $\sim T_e^{0.5}$ and others have weaker dependences on T_e. The intensity ratios of purely recombining plasma components for the transitions are nearly constant and almost independent on the electron temperature. So the temperature dependences of the line intensity ratios for ionization equilibrium plasma becomes weaker, comparing with the temperature dependences of those for purely ionizing plasma components. Some ratios of both ionizing plasma components and recombining plasma components, such as $R(20-5/45-9) = R(2s3d\ ^1D - 2s2p\ ^1P/2p3d\ ^1F - 2p^2\ ^1D)$, have weak dependences on the electron temperature, but the ratio with assuming the ion abundance ratio, $n(Fe^{23+})/n_1$, strongly depends on T_e. We expect that such ratios can be used to measure the ion abundance to check whether the plasma is in ionization equilibrium or not.

4.4 Radiative Power Loss

The radiative power loss due to line emissions is important to examine a plasma of $T_e \sim$ 1keV, since it is the dominant loss comparing to other processes such as the bremsstrahlung. The line radiation power loss per ion per electron per volume is obtained with

$$\begin{aligned} P_{line,I} &= \sum_{i,j} A_r(i,j) N_I(i) E(i,j)/n_e, \\ &= \sum_{i,j} C_I^{eff}(i,j) E(i,j), \end{aligned} \tag{27}$$

$$\begin{aligned} P_{line,R} &= \sum_{i,j} A_r(i,j) N_R(i) E(i,j)/n_e, \\ &= \sum_{i,j} C_R^{eff}(i,j) E(i,j), \end{aligned} \tag{28}$$

for ionizing plasma component and recombining plasma component, respectively. $E(i,j)$ is the energy of the transition. For ionizing plasma component it is the loss per Fe^{22+} ion and for recombining plasma component it is the loss per Fe^{23+} ion.

Total radiative loss due to Fe^{22+} ions is illustrated as a function of the electron temperature in Fig. 11a and as a function of electron density in Fig. 11b. The power loss by the ionizing plasma component slightly increases as the temperature increases, but the power loss by the recombining plasma component decreases. For a comparison the radiative power loss due to FeXXIV lines is plotted in Fig. 11a, which is about two times smaller than that due to FeXXIII lines.

The electron density dependence of the line radiation power loss is weak at $n_e \lesssim 10^{15}\mathrm{cm}^{-3}$. At higher density, $n_e \gtrsim 10^{20}\mathrm{cm}^{-3}$, both components of the power loss decrease with increasing density.

The power loss by the recombining plasma component is smaller than that by the ionizing plasma component for the equal ion abundances of Fe^{22+} and Fe^{23+} . The loss is enhanced slightly at higher temperature in the ionization-equilibrium plasma, compared to that in the ionizing plasma. If plasma is not in ionization equilibrium, the power loss due to the recombining plasma component would not be negligible at low electron temperature.

The power losses by the bremsstrahlung, the radiative recombination, and the satellite lines through the dielectronic recombination (from Fe^{23+} to Fe^{22+}) are also plotted in the Fig. 11a. The loss by the bremsstrahlung is calculated with

$$P_{brems} = 1.5 \times 10^{-25} T_e^{1/2} Z_{eff}^2 g_B \text{ erg s}^{-1}\text{cm}^3, \tag{29}$$

where T_e in eV, and the Gaunt factor, g_B, is assumed as unity. The ratio, $P_{brems}/P_{lines,I}$ is 7.7×10^{-3} at $T_e = 1$keV and $n_e = 10^{14}\text{cm}^{-3}$, when comparing with the loss by the ionizing plasma component.

The radiative recombination process emits continuum radiation through free-bound transitions. The loss is calculated with the photo-ionization cross section, which is taken from Clark et al. (1986) for $2snl$ ($n \leq 4$) states. For $2snl$ ($n \geq 5$) states the cross section is estimated with hydrogenic approximation as described in §3.3.2.

$$\begin{aligned} P_{rr} &= 1.05 \times 10^{-10} T_e^{-3/2} \sum_i \frac{g(i)}{g_0} \epsilon_i^4 e^{\chi_i} \int_1^\infty \sigma_i^{bf}(u) u^3 \exp(-\chi_i u) du \\ &\quad + \sum_{n \geq 5} 4.17 \times 10^{-19} \frac{Z^4}{n^3} T_e^{-1/2} \text{ erg s}^{-1}\text{cm}^3, \end{aligned} \tag{30}$$

where σ_i^{bf} in cm^{-2}. This loss is smaller by factor of 3 than the loss due to the bound-bound transitions of the recombining plasma component at $T_e = 1$keV.

The power loss by the satellite lines of the dielectronic recombination is calculated with eq.(14) as

$$P_{sat} = \sum_{i,j} C_s^{eff}(i,j) \Delta E(i,j), \tag{31}$$

where $\Delta E(i,j)$ is the transition energy from the auto-ionization states to the bound states and the summation is done for the all transitions considered in §3.3.1. At $T_e = 1$keV this loss is about factor 4 smaller than the loss by the bound-bound transitions of recombining plasma component.

5 Summary

We have constructed the collisional-radiative model for Fe^{22+} ions, taking into account the recombination processes from Fe^{23+} ions. We can treat high density plasma and non-equilibrium ionization plasma with our CRM. With this model we obtain the electron density and temperature dependences for the population densities of the excited states, the line intensities, the intensity ratios, and the radiative power loss due to the line emissions.

For astrophysical and laboratory plasmas where electron density is lower than 10^{20}cm^{-3}, the electron density dependences of the population densities and line intensities are small except for some levels affected by the metastable states with collisional excitation.

The line intensity ratios depend both on the electron temperature and ion abundance ratio of Fe^{23+} ion to Fe^{22+} ion. Since some ratios are sensitive to either the electron temperature and/or the abundance ratio, we can usethem to measure both these physical parameters.

References

[1] B. C. Fawcett, Physica Scripta, **24** (1981) 663

[2] E. Hinnov, S. Suckewer, S. Cohen, and K. Sato, Phys. Rev. A, **25** (1982) 2293

[3] J. Suger and W. L. Rowan, J. Opt. Soc. Am. B., **12** (1995) 1403

[4] D. W. Savin et al., Astrophys.J., **470** (1996) L73

[5] U. Feldman, Physica Scripta, **24** (1981) 681

[6] H. E. Mason, A. K. Bhatia, S. O. Kastner, W. M. Neupert, & M. Swartz, Sol. Phys., **92** (1984), 199

[7] D. L. McKenzie, P. B. Landecker, U. Feldman, and G. A. Doschek, Astrophys..J., **289** (1985) 849

[8] H. Matsumoto et al., Astrophys.J., **482** (1997) 133

[9] A. C. Fabian, K. A. Arnaud, M. W. Bautz, and Y. Tawara, Astrophys.J., **436** (1994) L63

[10] J. C. Raymond and B. W. Smith, Astrophys. J. Suppl., **35** (1977) 419

[11] R. Mewe, E. H. M. B. Gronenschild, G. H. J. van den Oord, Astron. Astrophys. Suppl., **62** (1985) 197

[12] D. A. Liedhal, A. L. Osterheld, W. H. Goldstein, Astrophys.J., **438** (1995) L115

[13] H. L. Zhang, D. H. Sampson, and R. E. H. Clark, Phys. Rev. A., **41** (1990) 198

[14] T. R. Kallman et al., Astrophys.J., **465** (1996) 994

[15] M. Arnaud and J. Raymond, Astrophys.J. **398** (1992) 394

[16] I. Murakami, T. Kato, and J. Dubou, NIFS-DATA 35 (1996)

[17] I. Murakami and T. Kato, Physica Scripta, **54** (1996) 463

[18] U. Safronova, I. Yu. Tolstikhina, R. Bruch, T. Tanaka, F. Hao, and D. Schneider, Physica Scripta, **47** (1993) 364

[19] H. Nussbaumer, and P. J. Storey, J. Phys. B., **12** (1979) 1647

[20] A. K. Bhatia and H. E. Mason, Astron. Astrophys., **103** (1981) 324

[21] H. L. Zhang, and D. H. Sampson, Atomic Data and Nucl. Data Tables, **52** (1992) 143

[22] D. H. Sampson, S. J. Goett, and R. E. H. Clark, Atomic Data and Nucl. Data Tables, **30** (1984) 125

[23] R. Mewe, Astron. Astrophys., **20**, 215 (1972)

[24] J. G. Doyle, Atomic Data and Nucl. Data Tables, **37** (1987) 441

[25] R. E. H. Clark, R. D. Cowan, and F. W. Bobrowicz, Atomic Data and Nucl. Data Tables **34** (1986) 415

[26] W. Lotz, Astrophys.J.Suppl., **14** (1967) 207

[27] T. Kato, U. I. Safronova, M. Ohira, Physica Scripta, **55** (1997) 185

[28] T. Shirai et al., J. Phys. Chem. Ref. Data, **19** (1990) 127

Table 1: Transition probabilities (A) and the wavelengths (λ), effective emission rate coefficients, of the selected transitions for $\lambda = 100 - 300$Å.

transition		A	λ	$C_I^{eff}(i,j)$†	$C_R^{eff}(i,j)$‡	λ‖
i–j		(s^{-1})	(Å)	(s^{-1})	(s^{-1})	(Å)
9–3	$2p^2\ ^1D_2$–$2s2p\ ^3P_1$	5.365E+08	118.68	3.672E-13	9.192E-14	121.20
5–1	$2s2p\ ^1P_0$–$2s^2\ ^1S_0$	2.003E+10	131.48	9.350E-10	2.330E-12	132.906[a]
9–4	$2p^2\ ^1D_2$–$2s2p\ ^3P_2$	5.403E+09	135.10	3.698E-12	9.257E-13	136.53
8–3	$2p^2\ ^3P_2$–$2s2p\ ^3P_1$	5.511E+09	142.86	6.462E-12	1.557E-12	144.36
7–2	$2p^2\ ^3P_1$–$2sp2\ ^3P_0$	6.654E+09	146.21	6.410E-12	1.375E-12	147.24
10–5	$2p^2\ ^1S_0$–$2s2p\ ^1P_0$	3.198E+10	147.94	1.805E-12	1.706E-13	149.22
7–3	$2p^2\ ^3P_1$–$2s2p\ ^3P_1$	4.139E+09	153.99	3.987E-12	8.552E-13	154.27
8–4	$2p^2\ ^3P_2$–$2s2p\ ^3P_2$	7.108E+09	167.33	8.334E-12	2.009E-12	166.74
6–3	$2p^2\ ^3P_0$–$2s2p\ ^3P_1$	1.183E+10	175.38	7.305E-13	1.386E-13	173.31
7–4	$2p^2\ ^3P_1$–$2s2p\ ^3P_2$	4.210E+09	182.81	4.056E-12	8.699E-13	180.10
9–5	$2p^2\ ^1D_2$–$2s2p\ ^1P_0$	4.477E+09	219.44	3.064E-12	7.671E-13	221.33
3–1	$2s2p\ ^3P_1$–$2s^2\ ^1S_0$	5.398E+07	267.62	5.139E-11	5.421E-12	263.765[a]
4–3	$2s2p\ ^3P_2$–$2s2p\ ^3P_1$	1.01E+04	976.78	4.723E-12	9.000E-13	1079.3[b]

5.365E+08 means 5.365×10^8.

† Effective emission rate coefficients for ionizing plasma component at $T_e = 1$keV and $n_e = 10^{14}$cm^{-3}.

‡ Effective emission rate coefficients for recombining plasma component at $T_e = 1$keV and $n_e = 10^{14}$cm^{-3}.

‖ Wavelength measured/calculated by others. Values are taken from Ref. [28] unless indicated. a from Ref. [3]. b from Ref. [2].

Table 2: Transition probabilities (A) and the wavelengths (λ), effective emission rate coefficients, of the selected transitions for $\lambda = 10.5 - 13$Å.

transition		A	λ	$C_I^{eff}(i,j)$	$C_R^{eff}(i,j)$	λ‖
i–j		(s^{-1})	(Å)	(s^{-1})	(s^{-1})	(Å)
35–4	$2p3p\ ^3P_2$–$2s2p\ ^3P_2$	4.514E+12	10.890	1.221E-13	5.208E-14	10.903
34–4	$2p3p\ ^3S_1$–$2s2p\ ^3P_2$	5.237E+12	10.893	6.108E-14	4.901E-14	
32–4	$2p3p\ ^3D_3$–$2s2p\ ^3P_2$	4.319E+12	10.914	1.913E-13	2.154E-13	
25–3	$2p3p\ ^3D_2$–$2s2p\ ^3P_1$	4.051E+12	10.919	1.510E-13	8.752E-14	10.935
15–1	$2s3p\ ^1P_1$–$2s^2\ ^1S_0$	7.388E+12	10.966	8.902E-12	1.887E-13	10.980
13–1	$2s3p\ ^3P_1$–$2s^2\ ^1S_0$	4.673E+12	11.006	4.713E-12	1.473E-13	
37–5	$2p3p\ ^1D_2$–$2s2p\ ^1P_0$	6.769E+12	11.156	1.790E-13	9.853E-14	11.166
17–2	$2s3d\ ^3D_1$–$2s2p\ ^3P_0$	1.297E+13	11.270	1.122E-12	1.811E-13	11.298
18–3	$2s3d\ ^3D_2$–$2s2p\ ^3P_1$	1.698E+13	11.308	2.528E-12	3.391E-13	11.325
17–3	$2s3d\ ^3D_1$–$2s2p\ ^3P_1$	9.414E+12	11.315	8.146E-13	1.314E-13	11.34
19–4	$2s3d\ ^3D_3$–$2s2p\ ^3P_2$	2.206E+13	11.429	5.261E-12	1.145E-12	11.442
18–4	$2s3d\ ^3D_2$–$2s2p\ ^3P_2$	5.524E+12	11.440	8.224E-13	1.103E-13	11.45
36–6	$2p3d\ ^3D_1$–$2p^2\ ^3P_0$	2.127E+13	11.465	2.647E-13	4.380E-14	11.519
39–7	$2p3d\ ^3P_2$–$2p^2\ ^3P_1$	1.048E+13	11.468	1.072E-13	6.912E-14	11.459
40–8	$2p3d\ ^3D_3$–$2p^2\ ^3P_2$	2.224E+13	11.501	2.277E-13	1.563E-13	11.525
45–9	$2p3d\ ^1F_3$–$2p^2\ ^1D_2$	3.348E+13	11.580	2.741E-13	3.512E-13	11.594
33–7	$2p3d\ ^1D_2$–$2p^2\ ^3P_1$	1.304E+13	11.596	8.094E-14	8.333E-14	11.614
11–2	$2s3s\ ^3S_1$–$2s2p\ ^3P_0$	3.869E+11	11.654	1.301E-13	3.869E-14	
31–8	$2p3d\ ^3F_3$–$2p^2\ ^3P_2$	7.098E+12	11.681	1.543E-13	2.561E-13	11.692
11–3	$2s3s\ ^3S_1$–$2s2p\ ^3P_1$	1.155E+12	11.701	3.883E-13	1.155E-13	
20–5	$2s3d\ ^1D_2$–$2s2p\ ^1P_0$	1.586E+13	11.725	2.746E-11	4.361E-13	11.737
29–8	$2p3d\ ^3F_2$–$2p^2\ ^3P_2$	1.684E+12	11.743	8.738E-14	1.157E-13	
24–7	$2p3s\ ^3P_2$–$2p^2\ ^3P_1$	1.005E+12	11.813	9.638E-14	8.706E-14	
11–4	$2s3s\ ^3S_1$–$2s2p\ ^3P_2$	2.029E+12	11.843	6.821E-13	2.029E-13	
22–6	$2p3s\ ^3P_1$–$2p^2\ ^3P_0$	8.685E+11	11.862	1.293E-13	4.095E-14	
46–10	$2p3d\ ^1P_1$–$2p^2\ ^1S_0$	2.041E+13	11.869	7.889E-13	5.842E-14	11.898
24–8	$2p3s\ ^3P_2$–$2p^2\ ^3P_2$	1.671E+12	11.884	1.603E-13	1.448E-13	
29–9	$2p3d\ ^3F_2$–$2p^2\ ^1D_2$	7.112E+11	11.943	3.690E-14	4.887E-14	
21–7	$2p3s\ ^3P_0$–$2p^2\ ^3P_1$	2.508E+12	12.002	9.326E-14	5.880E-14	12.095
27–9	$2p3s\ ^1P_1$–$2p^2\ ^1D_2$	2.102E+12	12.020	3.935E-13	8.656E-14	12.095
22–8	$2p3s\ ^3P_1$–$2p^2\ ^3P_2$	1.274E+12	12.048	1.897E-13	6.007E-14	
24–9	$2p3s\ ^3P_2$–$2p^2\ ^1D_2$	5.270E+11	12.089	5.054E-14	4.565E-14	
12–5	$2s3s\ ^1S_1$–$2s2p\ ^1P_0$	1.309E+12	12.149	1.244E-11	7.163E-14	
16–7	$2s3p\ ^3P_2$–$2p^2\ ^3P_1$	3.236E+10	12.345	4.727E-13	1.181E-13	
14–7	$2s3p\ ^3P_0$–$2p^2\ ^3P_1$	4.316E+10	12.402	4.344E-13	8.321E-14	
16–8	$2s3p\ ^3P_2$–$2p^2\ ^3P_2$	4.105E+10	12.423	5.996E-13	1.498E-13	
16–9	$2s3p\ ^3P_2$–$2p^2\ ^1D_2$	9.272E+09	12.647	1.354E-13	3.383E-14	
15–9	$2s3p\ ^1P_1$–$2p^2\ ^1D_2$	2.183E+11	12.653	2.631E-13	5.576E-15	12.65

‖ Wavelength taken from Ref. [28].

Table 3: Transition probabilities (A) and the wavelengths (λ), effective emission rate coefficients, of the selected transitions for $\lambda = 6 - 10$Å.

transition		A	λ	$C_I^{eff}(i,j)$	$C_R^{eff}(i,j)$	$\lambda^\sharp$
i–j		(s^{-1})	(Å)	(s^{-1})	(s^{-1})	(Å)
268–1	2s10p ^{1}P–2s^2 ^{1}S$_0$	3.654E+11	6.599	3.486E-14	5.172E-16	
230–1	2s9p ^{1}P–2s^2 ^{1}S$_0$	4.854E+11	6.659	4.995E-14	2.399E-15	
196–1	2s8d ^{3}D–2s^2 ^{1}S$_0$	6.580E+11	6.746	7.354E-14	1.863E-15	
165–1	2s7p ^{1}P–2s^2 ^{1}S$_0$	8.923E+11	6.877	9.727E-14	2.309E-15	
270–5	2s10d ^{1}D–2s2p ^{1}P$_1$	2.684E+11	6.946	3.588E-14	1.035E-15	
232–5	2s9d ^{1}D–2s2p ^{1}P$_1$	3.817E+11	7.012	5.376E-14	3.953E-15	
166–4	2s7d ^{3}D–2s2p ^{3}P$_2$	6.033E+11	7.106	1.015E-14	1.052E-14	
198–5	2s8d ^{1}D–2s2p ^{1}P$_1$	5.609E+11	7.108	8.218E-14	3.509E-15	
163–5	2s7s ^{1}S–2s2p ^{1}P$_1$	1.247E+11	7.262	1.036E-14	1.161E-15	
139–3	2s6d ^{3}*D*–2s2p ^{3}P$_1$	5.710E+11	7.276	1.125E-14	1.123E-14	
139–4	2s6d ^{3}*D*–2s2p ^{3}P$_2$	9.274E+11	7.331	1.827E-14	1.823E-14	
183–9	2p6d ^{1}F–2p^2 ^{1}D$_2$	3.040E+12	7.447	1.174E-14	1.987E-14	
102–1	2s5p ^{1}P–2s^2 ^{1}S$_0$	1.663E+11	7.472	5.279E-13	1.191E-14	7.472
140–5	2s6d ^{1}D–2s2p ^{1}P$_1$	1.687E+12	7.484	2.998E-13	1.100E-14	
136–5	2s6s ^{1}S–2s2p ^{1}P$_1$	3.566E+11	7.502	3.884E-14	2.890E-15	
103–2	2s5d ^{3}D–2s2p ^{3}P$_0$	3.604E+11	7.657	1.080E-14	8.430E-15	
103–3	2s5d ^{3}D–2s2p ^{3}P$_1$	1.066E+12	7.677	3.194E-14	2.494E-14	
143–9	2s6d ^{1}F–2p^2 ^{1}D$_2$	2.434E+10	7.746	1.485E-14	9.330E-16	
128–9	2p5d ^{1}F–2p^2 ^{1}D$_2$	5.375E+12	7.863	3.343E-14	3.620E-14	7.849
138–10	2s6p ^{1}P–2p^2 ^{1}S$_0$	1.182E+11	7.892	1.670E-14	3.810E-16	
104–5	2s5d ^{1}D–2s2p ^{1}P$_1$	2.941E+12	7.906	7.442E-13	2.519E-14	7.883
100–5	2s5s ^{1}S–2s2p ^{1}P$_1$	4.811E+11	7.943	8.718E-14	4.453E-15	
133–10	2p5d ^{1}P–2p^2 ^{1}S$_0$	2.998E+12	8.000	1.277E-14	6.978E-15	
79–4	2p4p ^{3}D$_3$–2s2p ^{3}P$_2$	2.240E+12	8.266	1.762E-14	3.140E-14	8.273
52–1	2s4p ^{1}P$_1$–2s^2 ^{1}S$_0$	4.137E+12	8.293	1.609E-12	4.745E-14	8.305
50–1	2s4p ^{3}P$_1$–2s^2 ^{1}S$_0$	9.146E+11	8.306	2.349E-13	2.982E-14	8.317
102–10	2s5p ^{1}P–2p^2 ^{1}S$_0$	9.700E+10	8.371	2.016E-14	4.551E-16	
53–2	2s4d ^{3}D$_1$–2s2p ^{3}P$_0$	3.715E+12	8.510	7.819E-14	2.676E-14	8.529
56–3	2s4d ^{1}D$_2$–2s2p ^{3}P$_1$	2.808E+10	8.517	1.223E-14	4.141E-16	
54–3	2s4d ^{3}D$_2$–2s2p ^{3}P$_1$	4.985E+12	8.534	1.554E-13	5.843E-14	8.550
53–3	2s4d ^{3}D$_1$–2s2p ^{3}P$_1$	2.694E+12	8.535	5.670E-14	1.941E-14	
55–4	2s4d ^{3}D$_3$–2s2p ^{3}P$_2$	6.614E+12	8.606	3.333E-13	1.198E-13	8.616
54–4	2s4d ^{3}D$_2$–2s2p ^{3}P$_2$	1.624E+12	8.609	5.062E-14	1.904E-14	
47–3	2s4s ^{3}S$_1$–2s2p ^{3}P$_1$	2.811E+11	8.621	2.934E-14	1.279E-14	
70–6	2p4d ^{3}D$_1$–2p^2 ^{3}P$_0$	6.580E+12	8.653	2.582E-14	9.044E-15	
84–8	2p4d ^{3}D$_3$–2p^2 ^{3}P$_2$	5.864E+12	8.660	1.764E-14	3.607E-14	8.672

♯ Wavelength taken from Ref. [28].

Table 3 ... continued

transition		A	λ	$C_I^{eff}(i,j)$	$C_R^{eff}(i,j)$	$\lambda^\sharp$
i–j		(s^{-1})	(Å)	(s^{-1})	(s^{-1})	(Å)
47–4	2s4s ^{3}S$_1$–2s2p ^{3}P$_2$	5.656E+11	8.698	5.904E-14	2.573E-14	
68–7	2p4d ^{1}D$_2$–2p^2 ^{3}P$_1$	5.500E+12	8.719	1.210E-14	2.227E-14	8.643
95–9	2p4d ^{1}F$_3$–2p^2 ^{1}D$_2$	1.147E+13	8.747	3.718E-14	8.888E-14	8.752
69–8	2p4d ^{3}F$_3$–2p^2 ^{3}P$_2$	4.524E+12	8.755	1.642E-14	5.216E-14	8.763
56–5	2s4d ^{1}D$_2$–2s2p ^{1}P$_1$	5.777E+12	8.807	2.516E-12	8.519E-14	8.815
48–5	2s4s ^{1}S$_0$–2s2p ^{1}P$_0$	6.535E+11	8.900	4.935E-13	1.312E-14	8.906
97–10	2p4d ^{1}P$_1$–2p^2 ^{1}S$_0$	6.591E+12	8.915	4.360E-14	1.503E-14	
60–9	2s4f ^{1}F$_3$–2p^2 ^{1}D$_2$	1.224E+10	9.166	2.154E-14	7.480E-16	
52–9	2s4p ^{1}P$_1$–2p^2 ^{1}D$_2$	4.810E+10	9.224	1.871E-14	5.517E-16	
52–10	2s4p ^{1}P$_1$–2p^2 ^{1}S$_0$	1.114E+11	9.415	4.333E-14	1.278E-15	

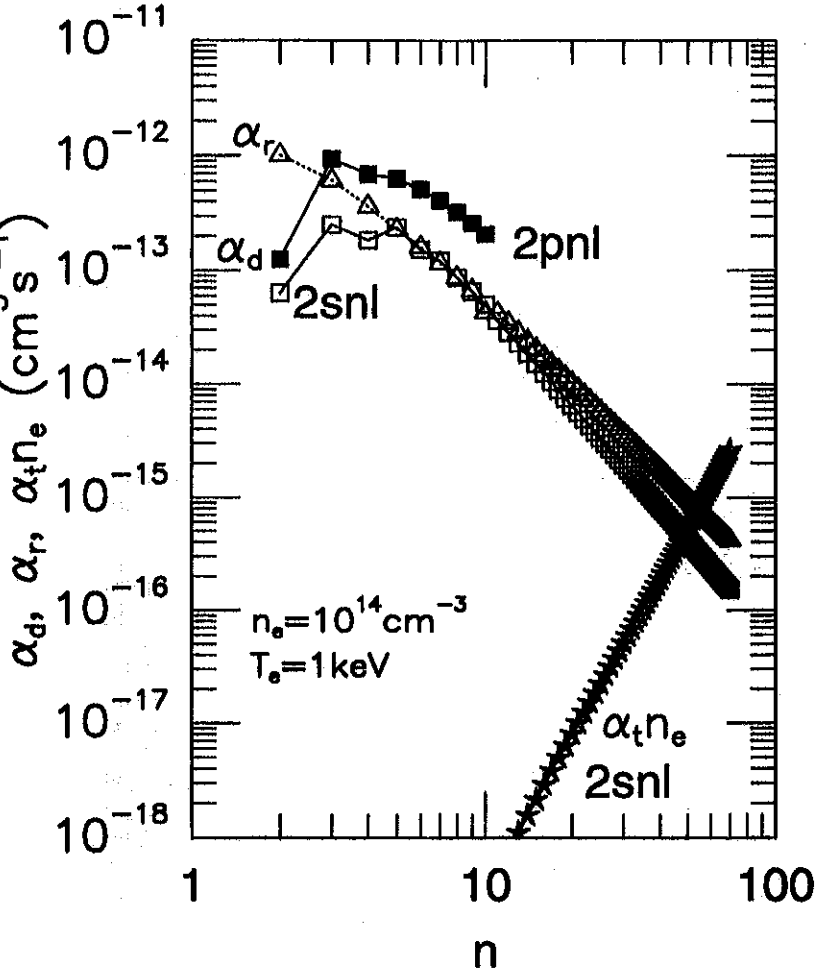

Figure 1: The dielectronic recombination rate coefficients to 2s*nl* and 2p*nl* levels, the radiative recombination rate coefficients, and the three body recombination rate coefficients, are ploted as a function of the principal quantum number,*n*, at the electron temperature of 1keV.

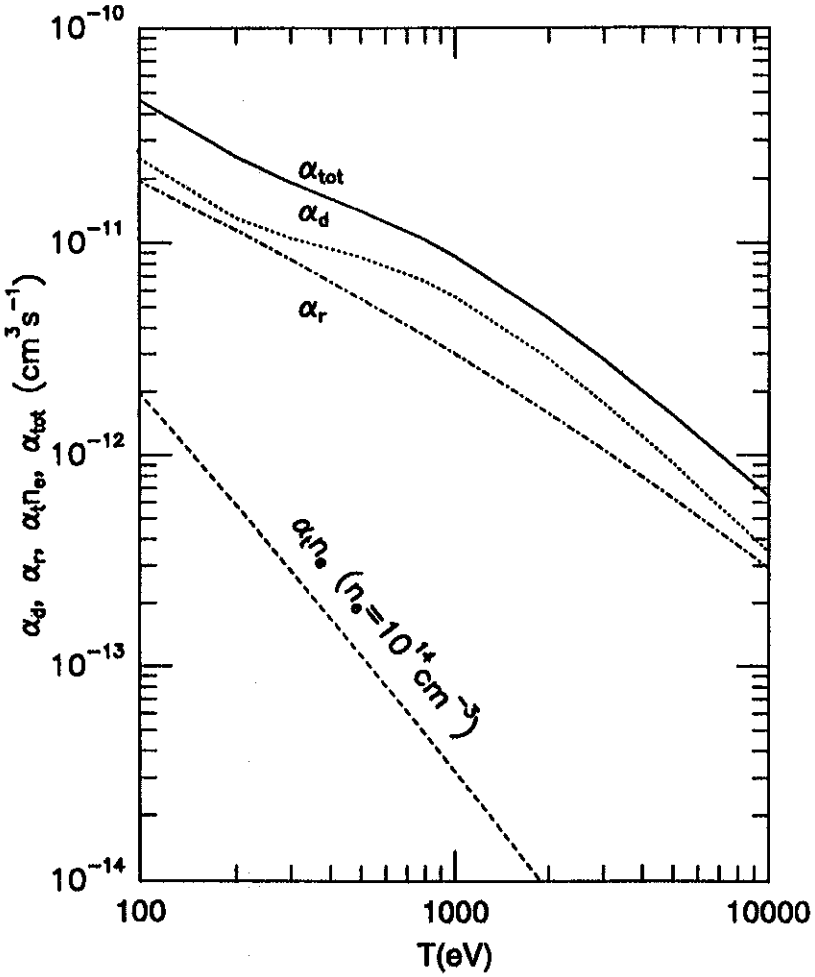

Figure 2: Electron temperature dependences of total recombination rate, total dielectronic recombination rate, radiative recombination rate, and three body recombination rate, at the electron density of $10^{14}cm^{-3}$. The rate coefficients up to $n = 70$ are added as total.

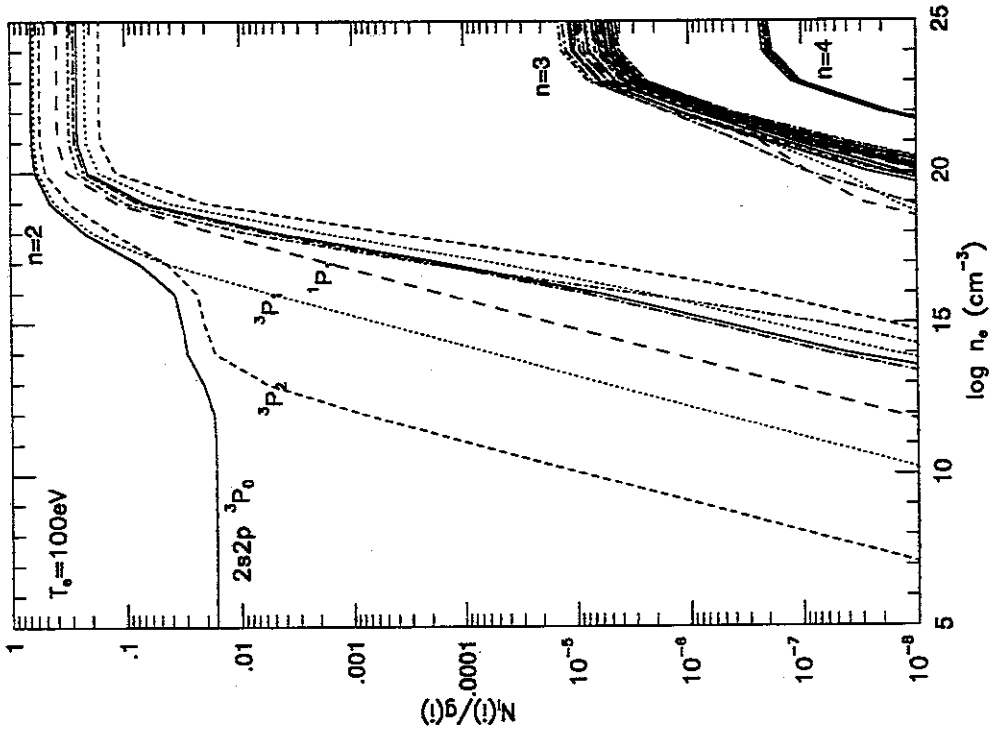

Figure 3: (b) For T_e = 100eV.

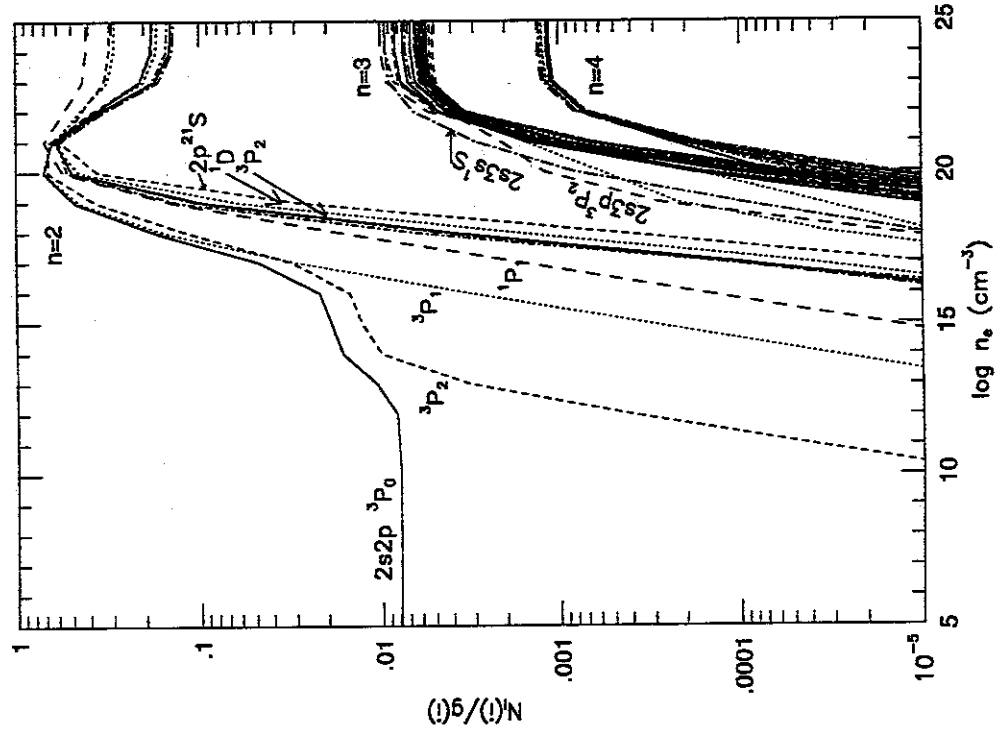

Figure 3: (a) The electron density dependence of excited state population density of ionizing plasma component, devided by g_i for T_e = 1keV.

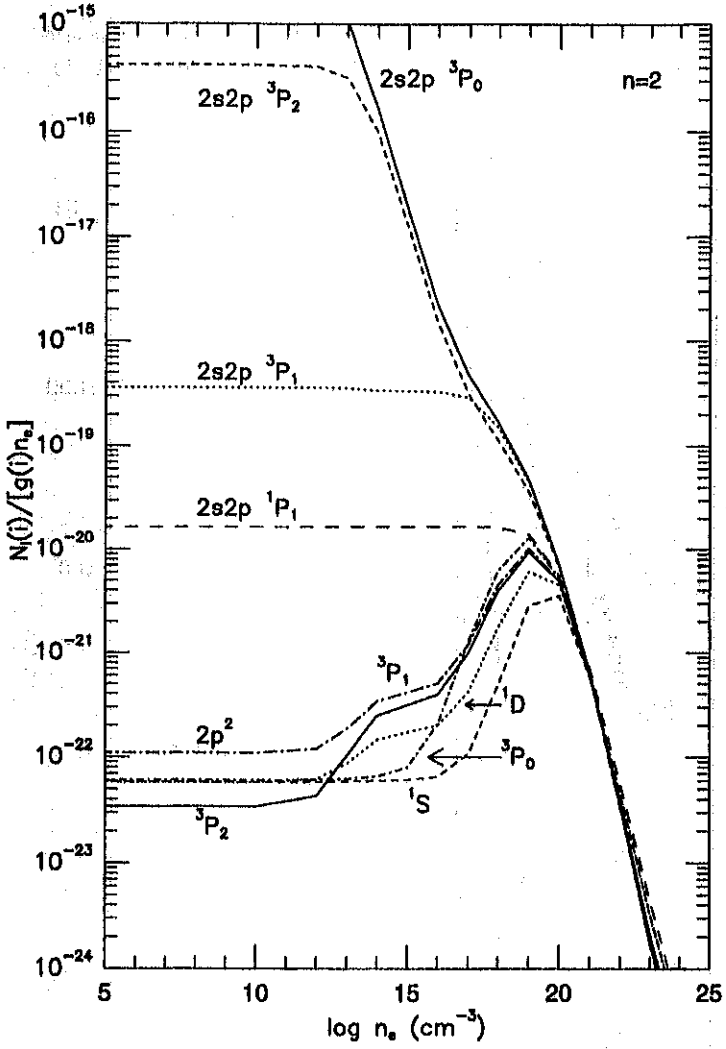

Figure 4: (a) The electron density dependence of excited state population densities of ionizing plasma component, devided by $g_i n_e$ for $n = 2$ levels at $T_e = 1$keV.

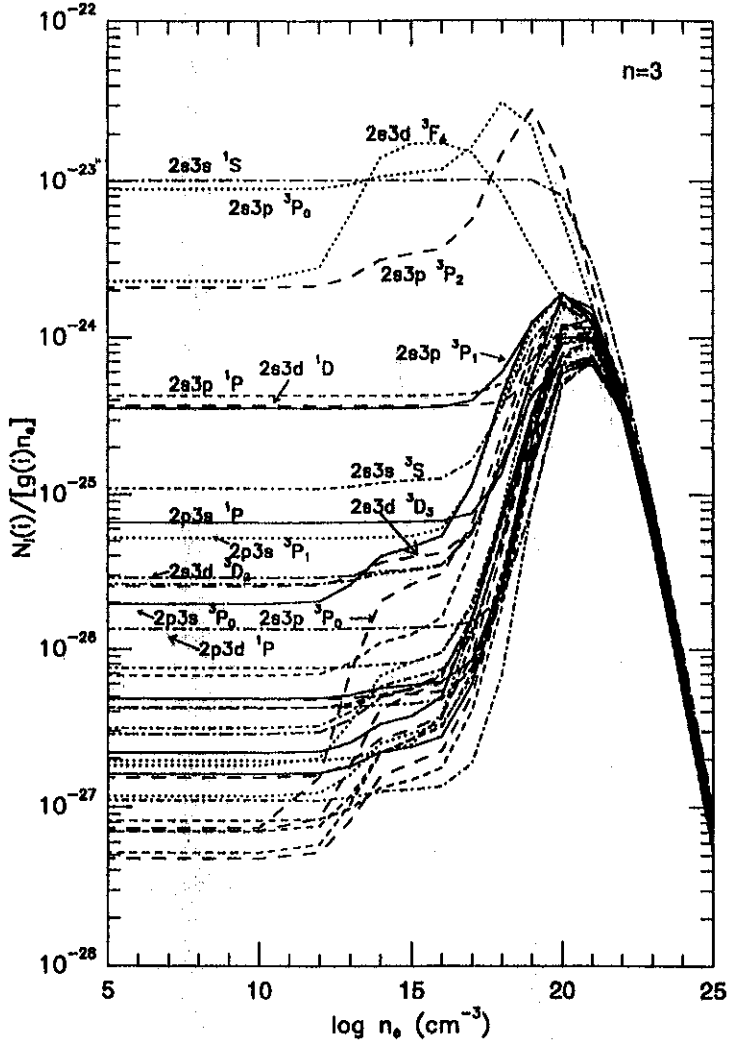

Figure 4: (b) For $n = 3$ levels at $T_e = 1$keV.

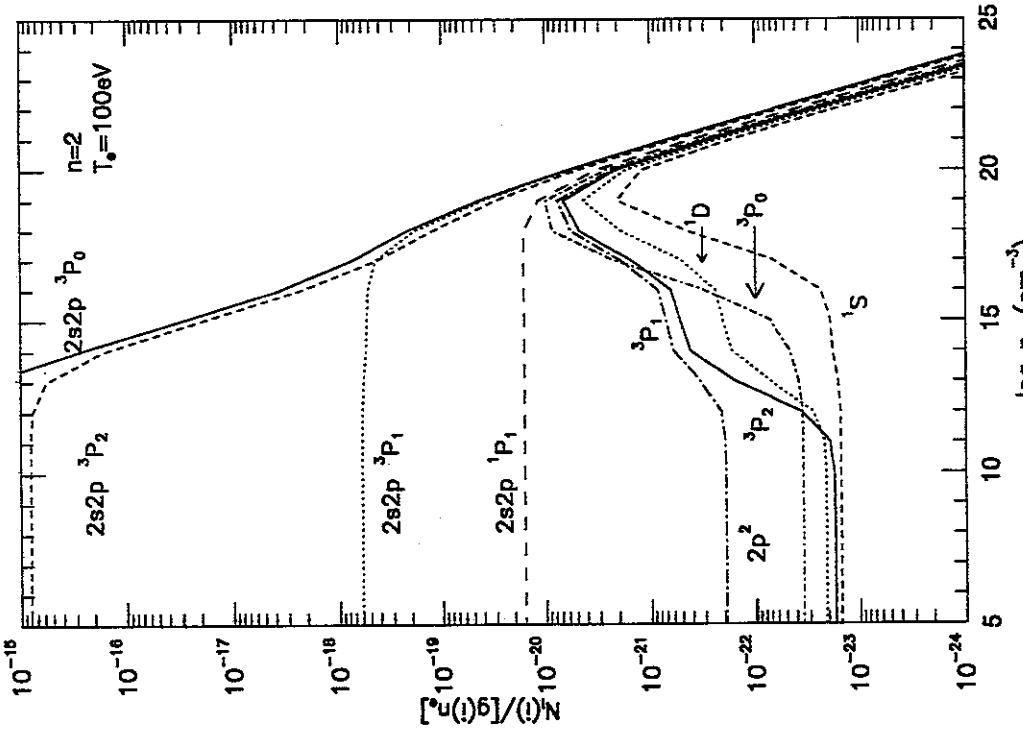

Figure 4: (d) For $n = 2$ levels at $T_e = 100$eV.

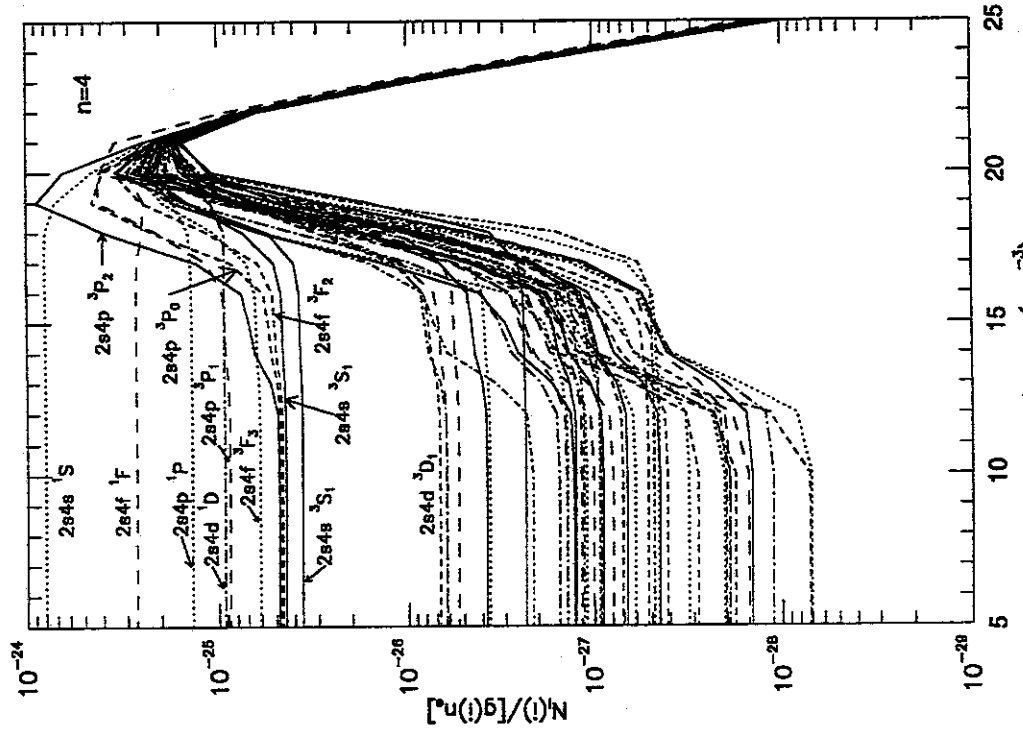

Figure 4: (c) For $n = 4$ levels at $T_e = 1$keV.

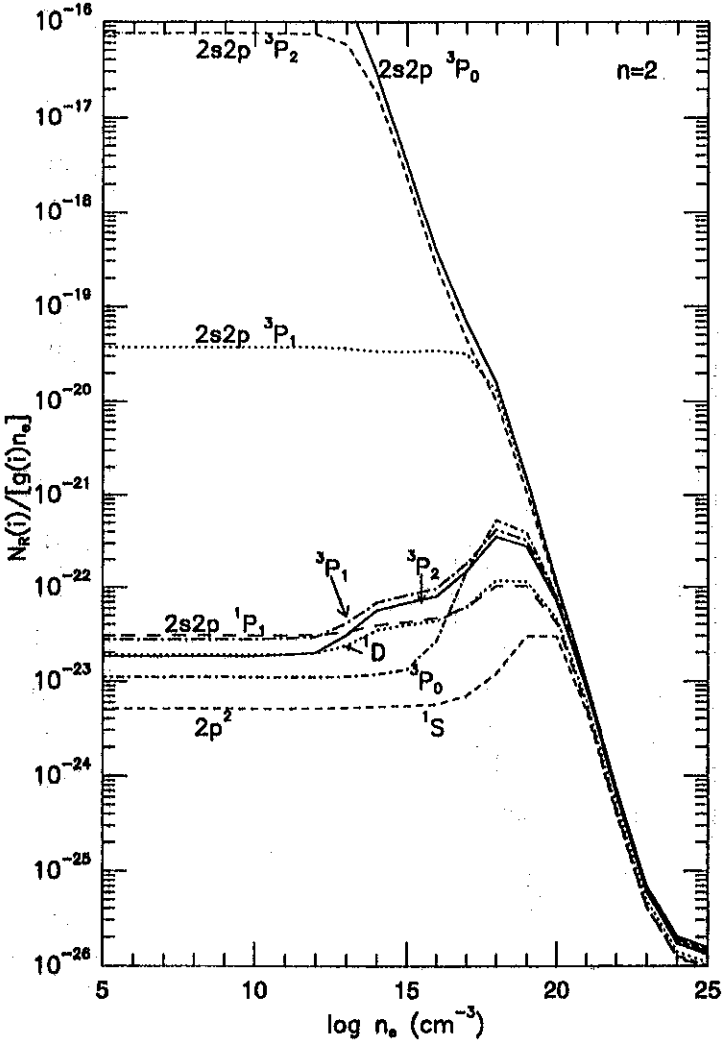

Figure 5: (a) The electron density dependence of excited state population densities of recombining plasma component, devided by $g_i n_e$ for $n = 2$ levels at $T_e = 1$keV.

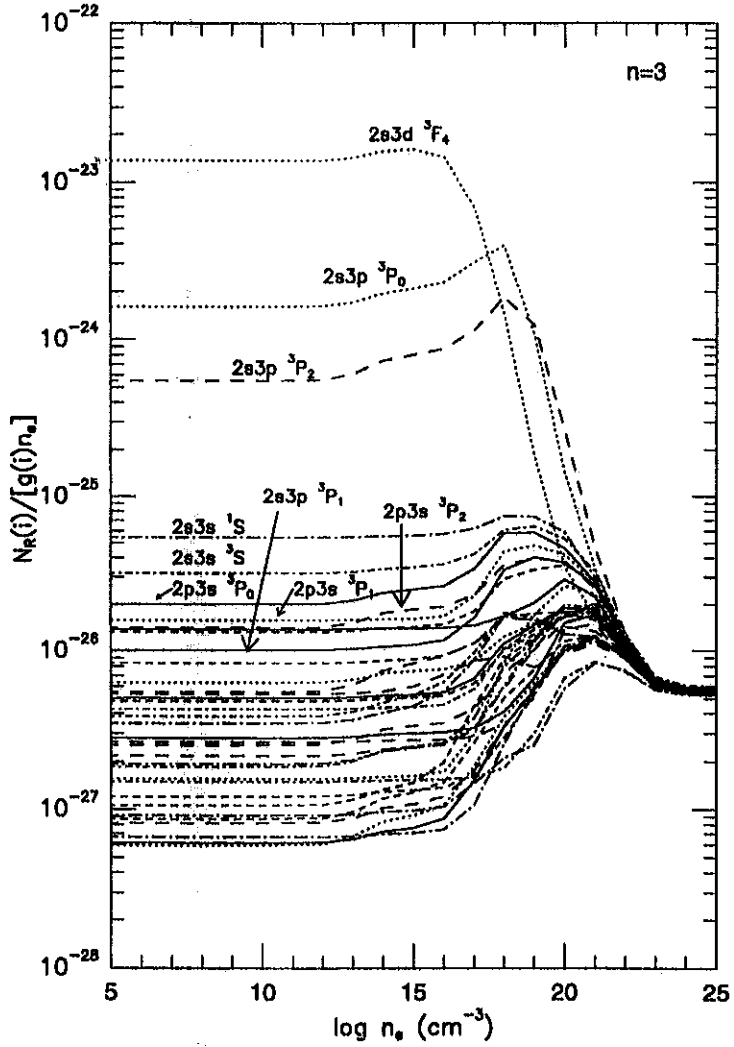

Figure 5: (b) For $n = 3$ levels at $T_e = 1$keV.

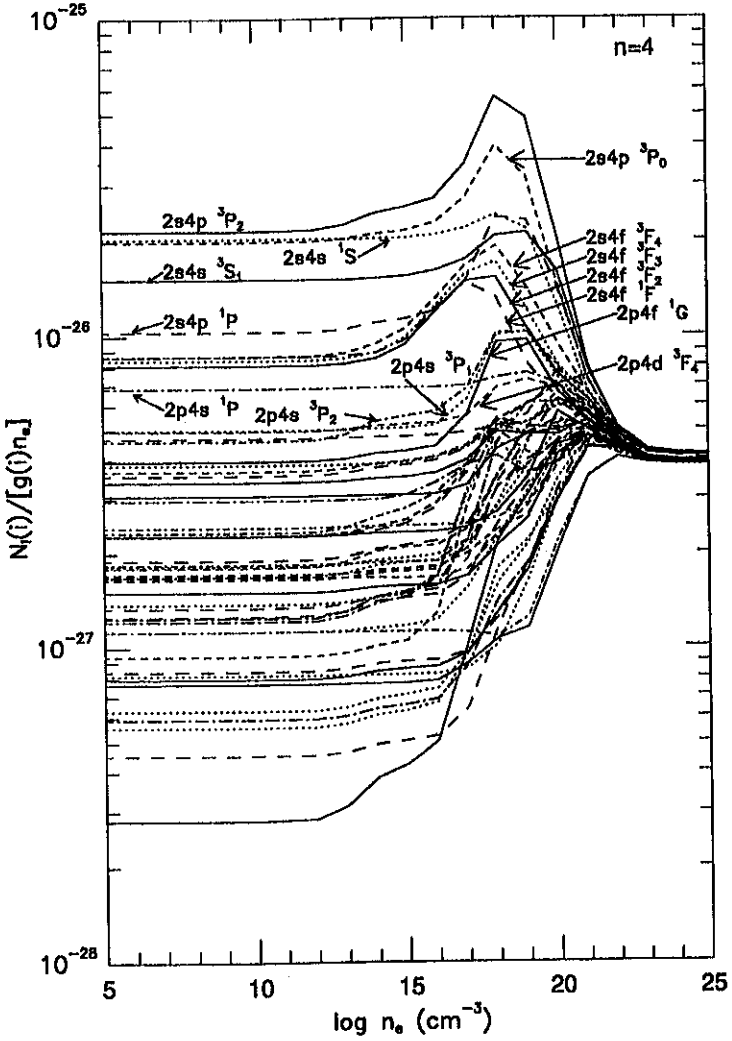

Figure 5: (c) For $n = 4$ levels at $T_e = 1$keV.

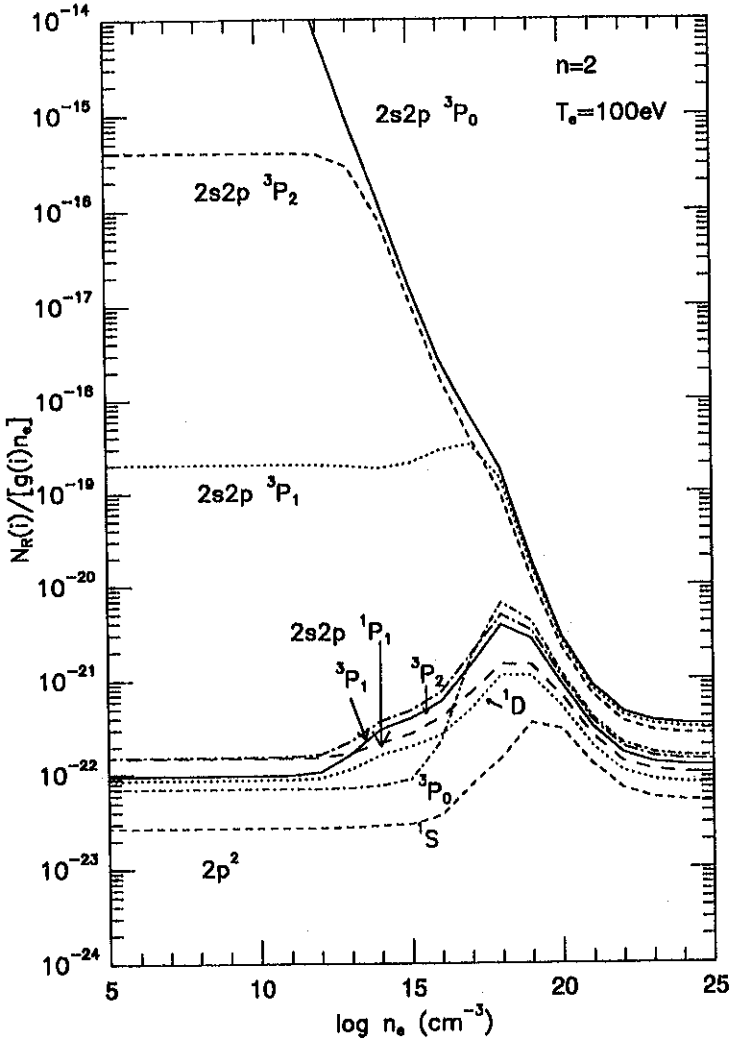

Figure 5: (d) For $n = 2$ levels at $T_e = 100$eV.

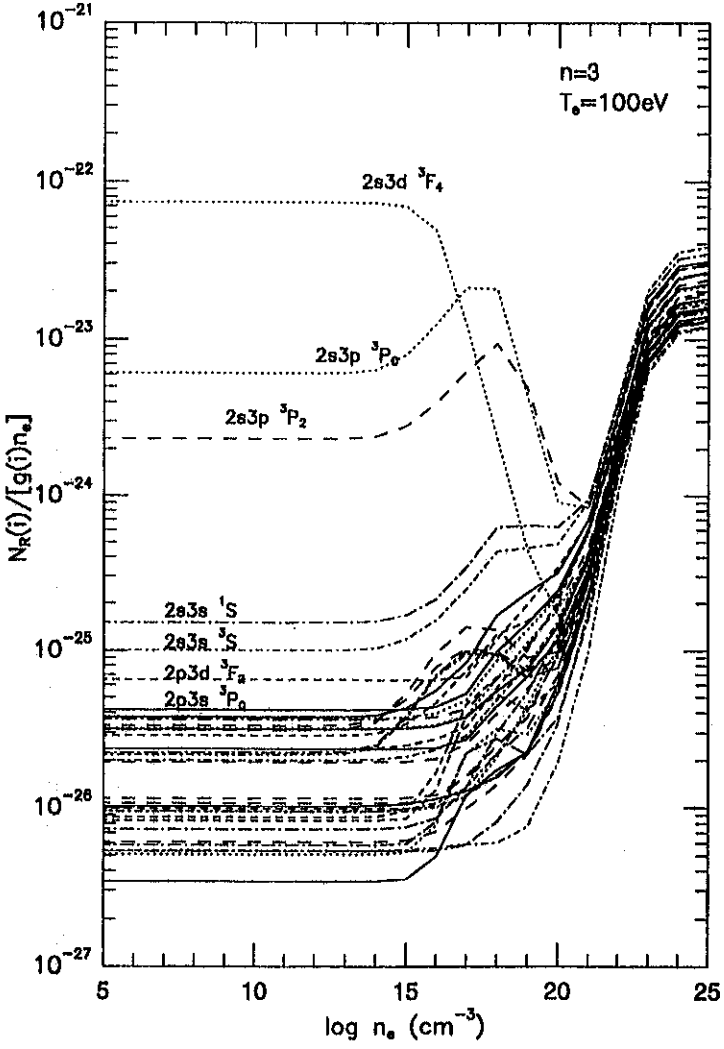

Figure 5: (e) For $n = 3$ levels at $T_e = 100$eV.

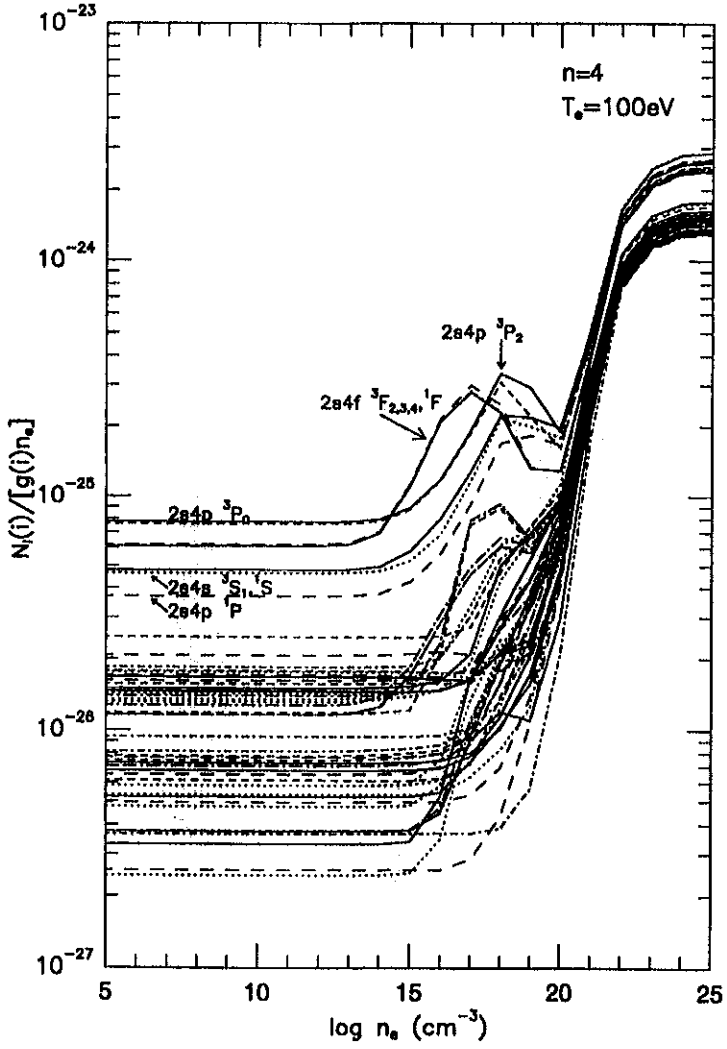

Figure 5: (f) For $n = 4$ levels at $T_e = 100$eV.

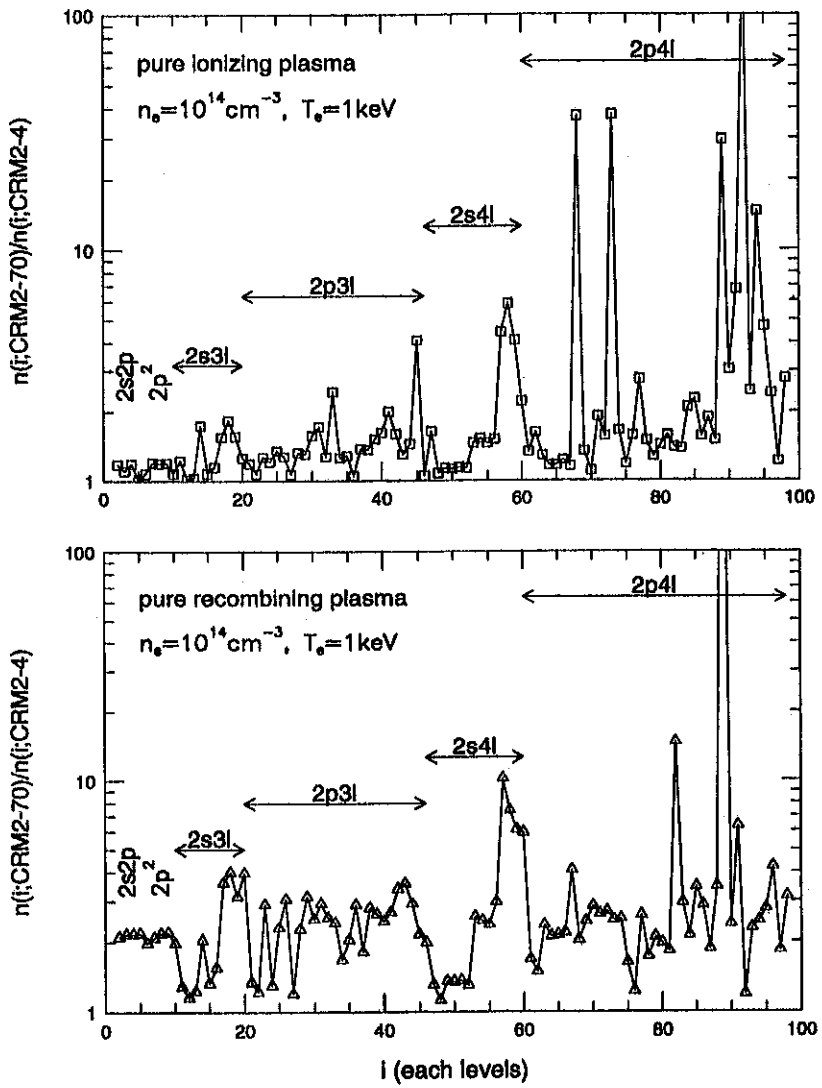

Figure 6: (a) The ratio of population density calculated by CRM with $n \leq 70$ to population density calculated by CRM with $n \leq 4$ for each level with $n \leq 4$, where n is the principal quantum number. at $n_e = 10^{14}\text{cm}^{-3}$ and $T_e = 1\text{keV}$. Upper panel shows for ionizing plasma component and lower panel shows for recombining plasma component.

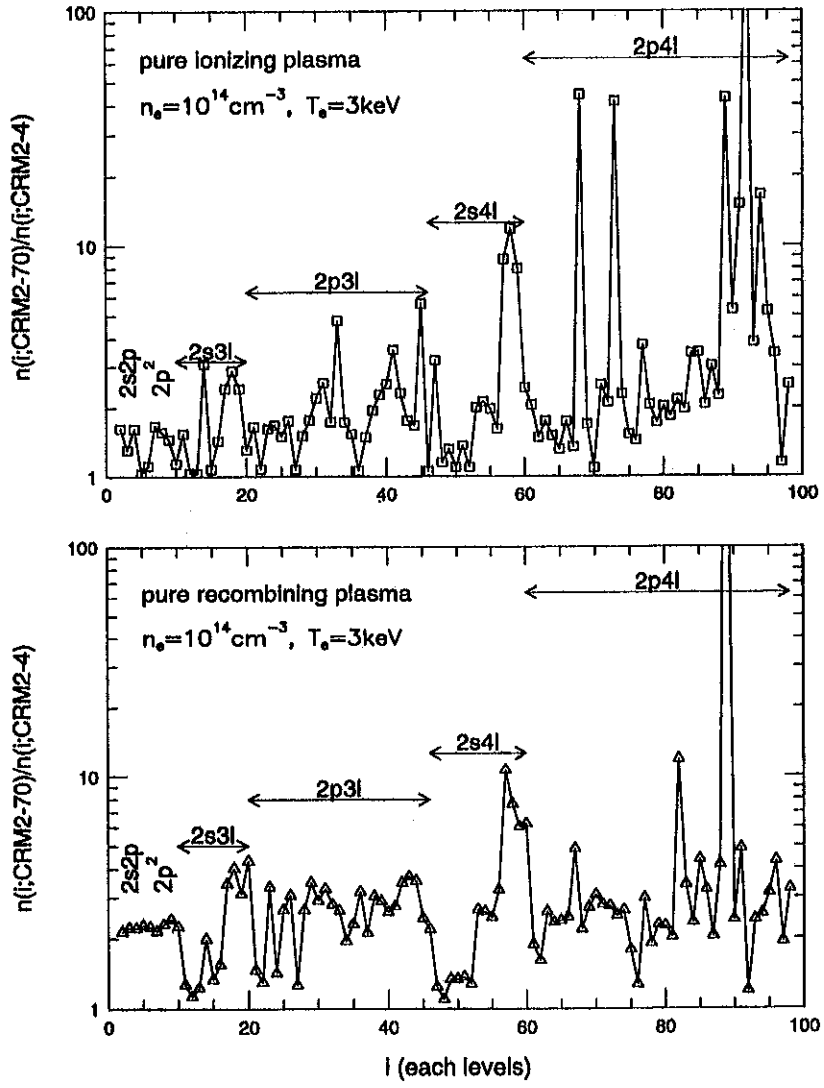

Figure 6: (b) For $T_e = 3\text{keV}$ and $n_e = 10^{14}\text{cm}^{-3}$.

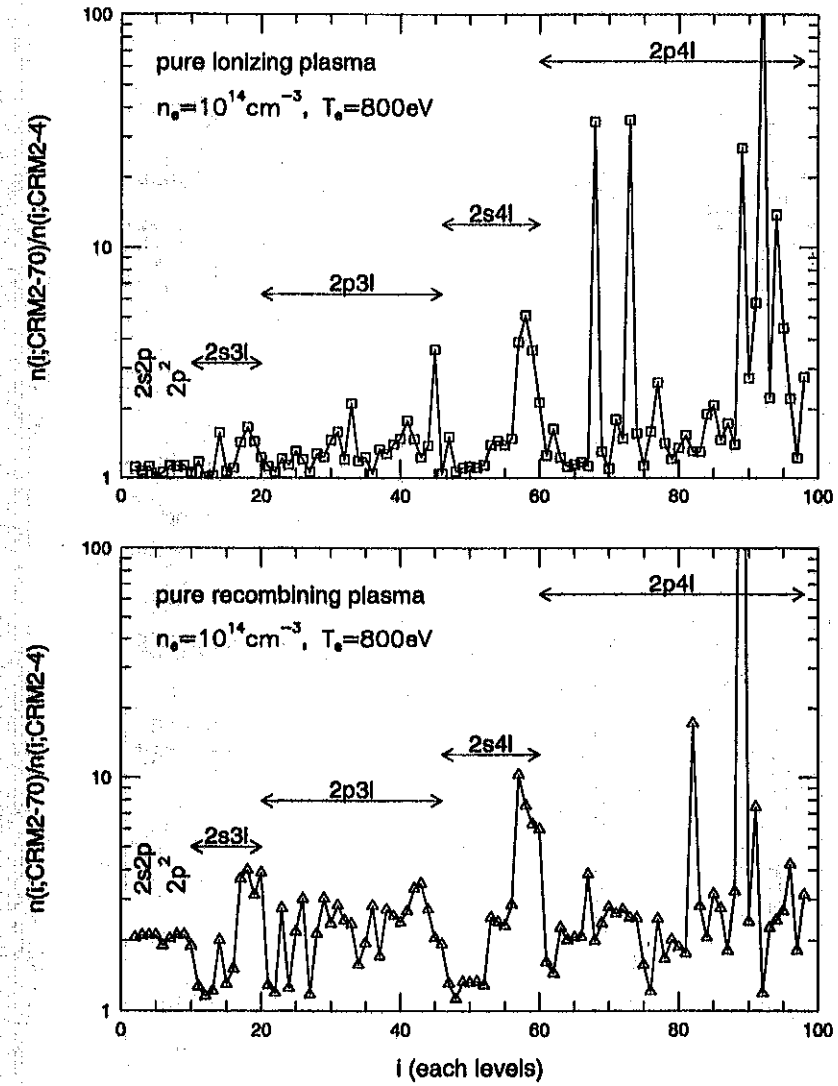

Figure 6: (c) For $T_e = 800$eV and $n_e = 10^{14}$cm^{-3}.

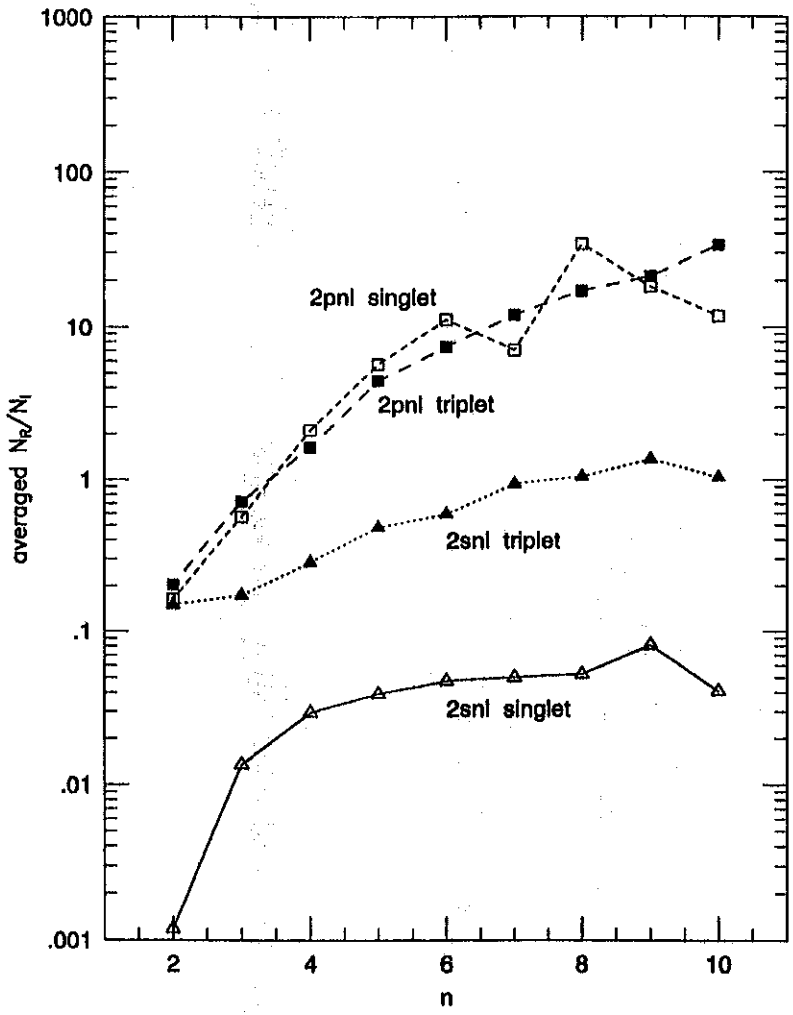

Figure 7: The averaged ratio of population densities of recombining plasma component to ionizing plasma component as a function of principal quantum number, n, at $n_e = 10^{14}$cm^{-3} and $T_e = 1$keV.

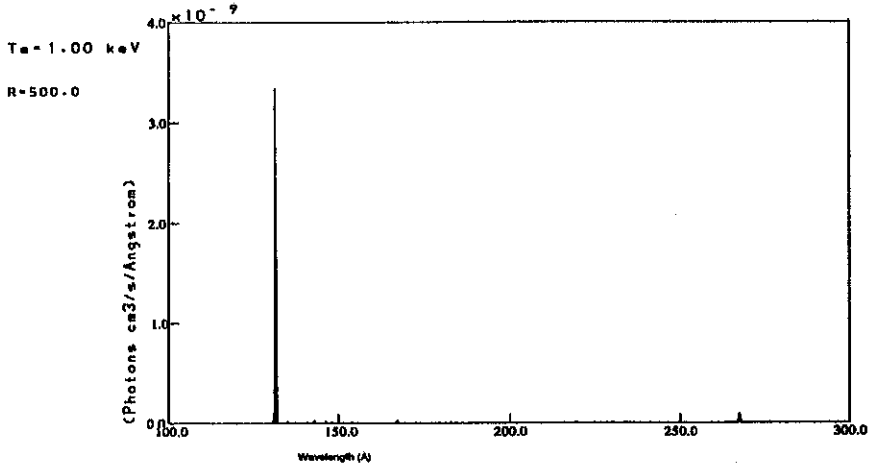

Figure 8: (a) Calculated FeXXIII spectrum of ionizing plasma component at $n_e = 10^{14}\text{cm}^{-3}$ and $T_e = 1\text{keV}$ for $\lambda = 100 - 300$ Å. Resolving power, $R = \lambda/\Delta\lambda = 500$ is assumed to produce Gaussian profile.

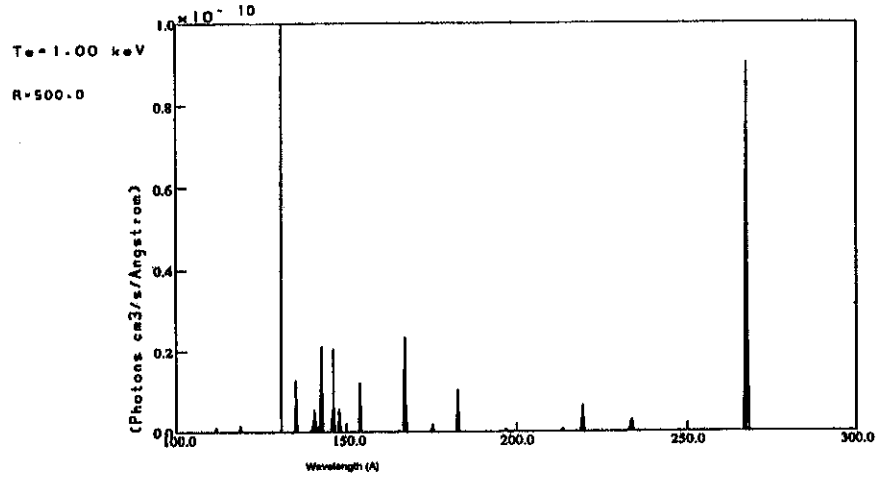

Figure 8: (b) Close up of (a).

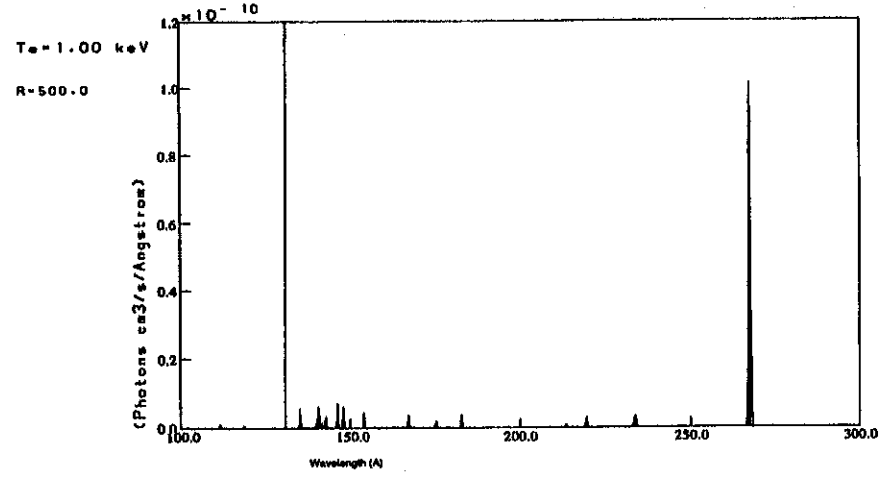

Figure 8: (c) Same as (b) but for $n_e = 10^{11}\text{cm}^{-3}$ ($T_e = 1\text{keV}$; ionizing plasma component.)

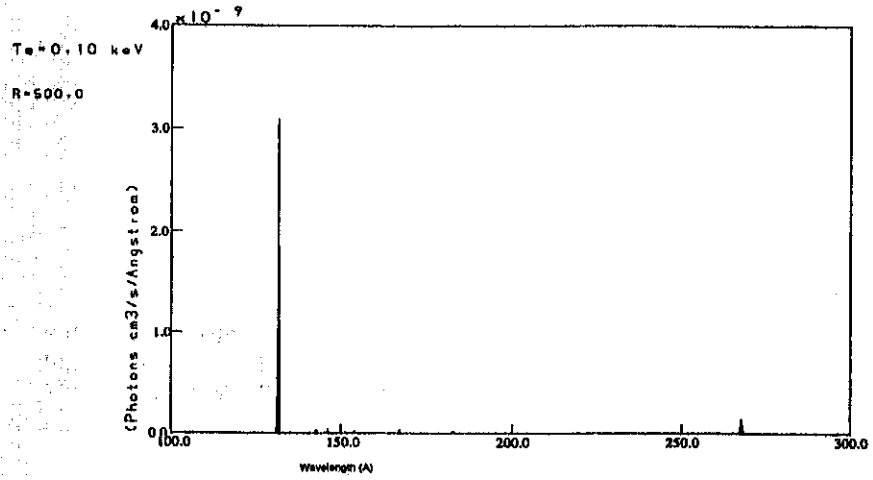

Figure 8: (d) Same as (a) but for $T_e = 100$eV ($n_e = 10^{14}$cm^{-3}; ionizing plasma component).

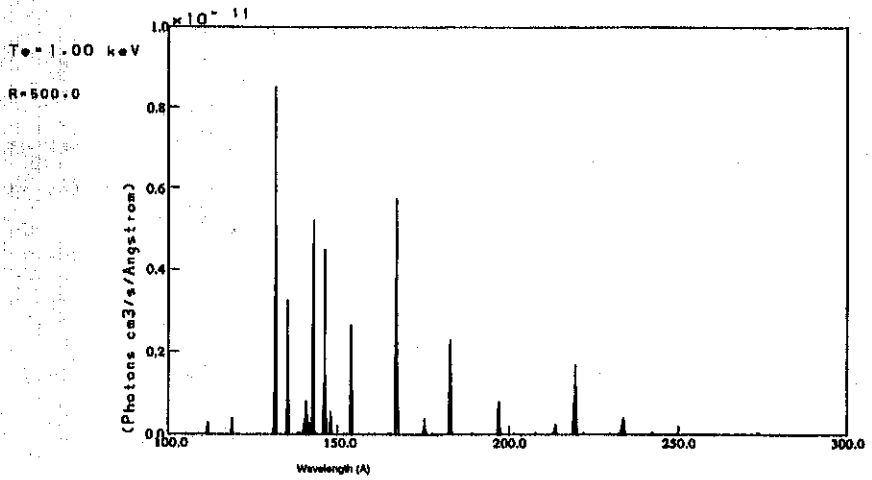

Figure 8: (e) Same as (a) but for recombining plasma component ($T_e = 1$keV, $n_e = 10^{14}$cm^{-3}).

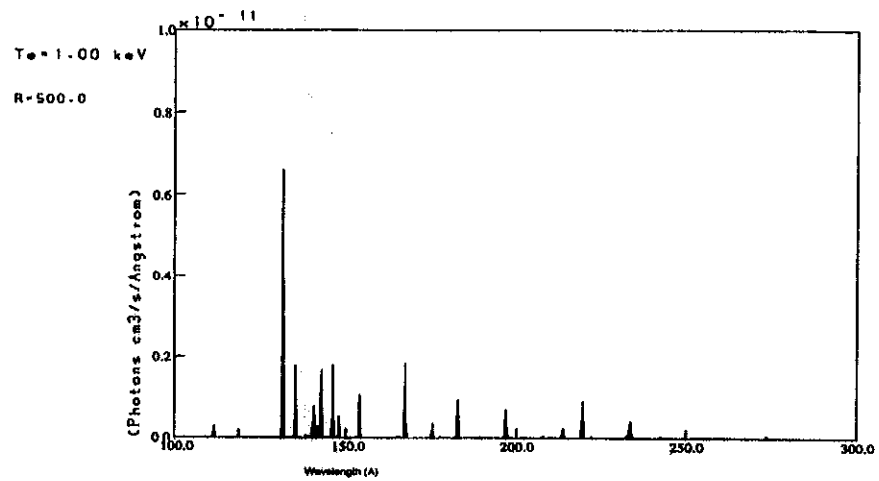

Figure 8: (f) Same as (e) but for $n_e = 10^{11}$cm^{-3} ($T_e = 1$keV; recombining plasma component.)

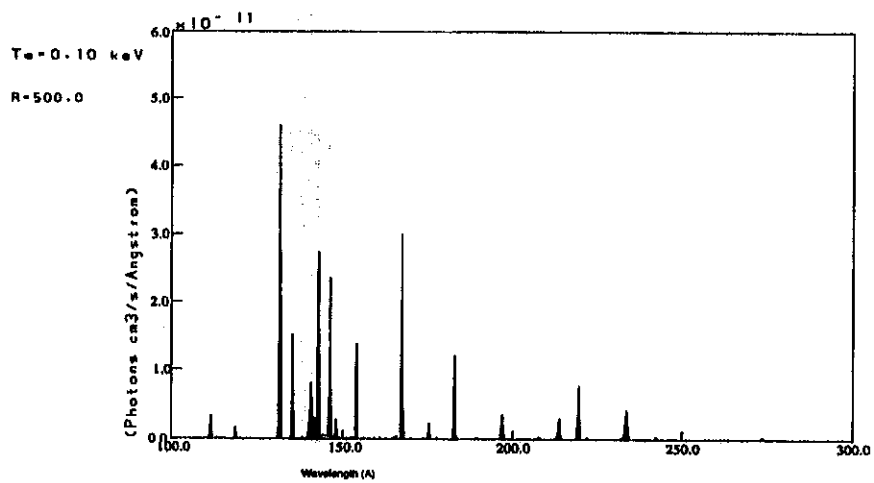

Figure 8: (g) Same as (e) but for $T_e = 100$eV ($n_e = 10^{14}$cm^{-3}; recombining plasma component).

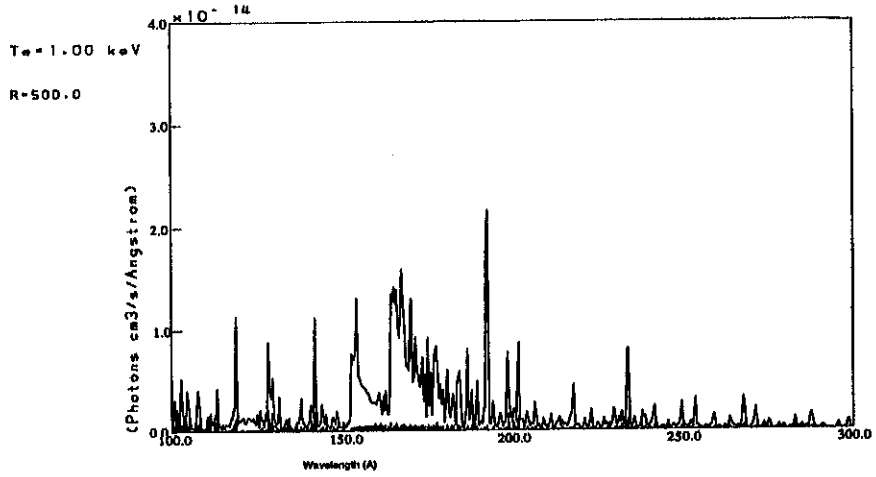

Figure 8: (h) Dielectronic satellite lines for the same plasma as (e) (T_e = 1keV, n_e = 10^{14}cm^{-3}).

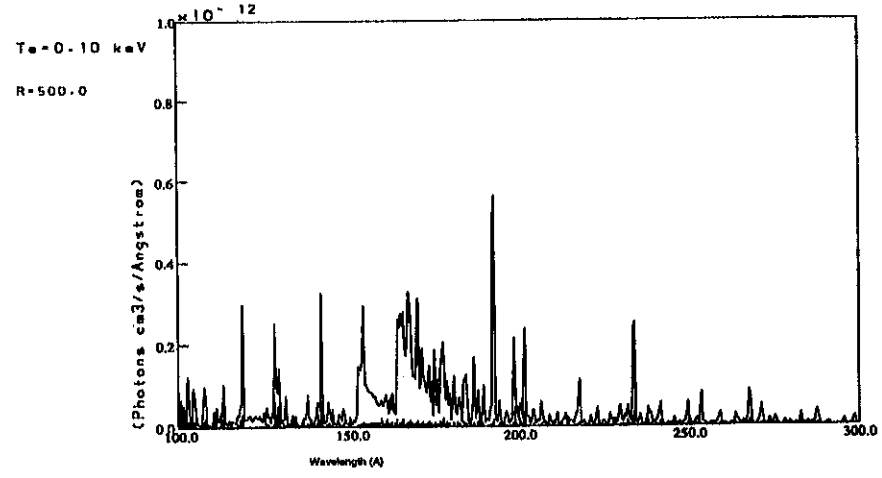

Figure 8: (i) Same as (h) but for T_e = 100eV (n_e = 10^{14}cm^{-3}).

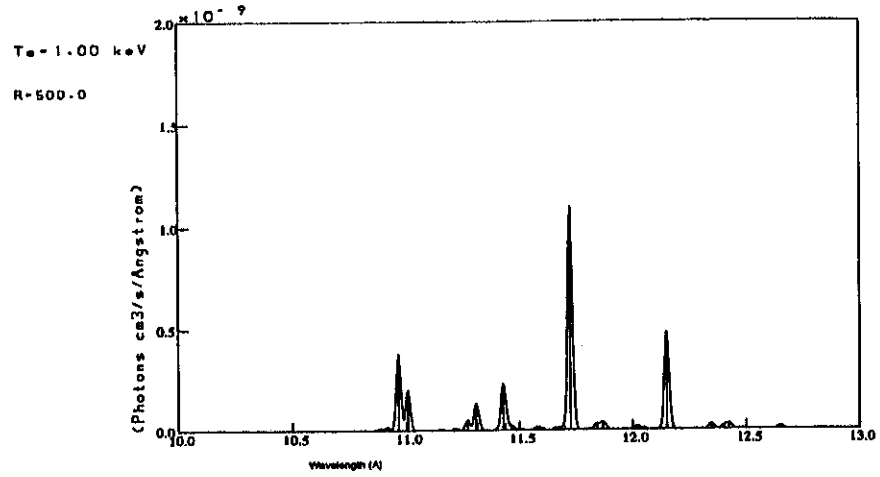

Figure 8: (j) Same as (a) but for $\lambda = 10 - 13$ Åregion (ionizing plasma component; T_e = 1keV, n_e = 10^{14}cm^{-3}).

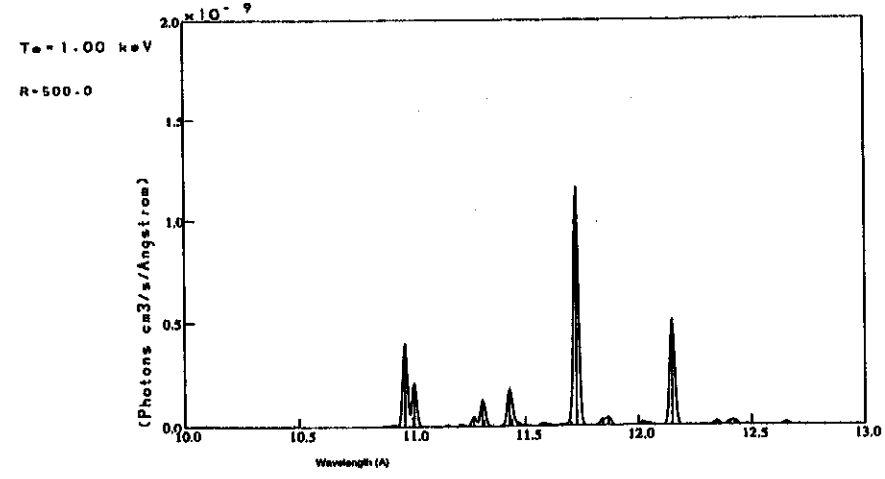

Figure 8: (k) Same as (j) but for $n_e = 10^{11}$cm^{-3} (T_e = 1keV; ionizing plasma component).

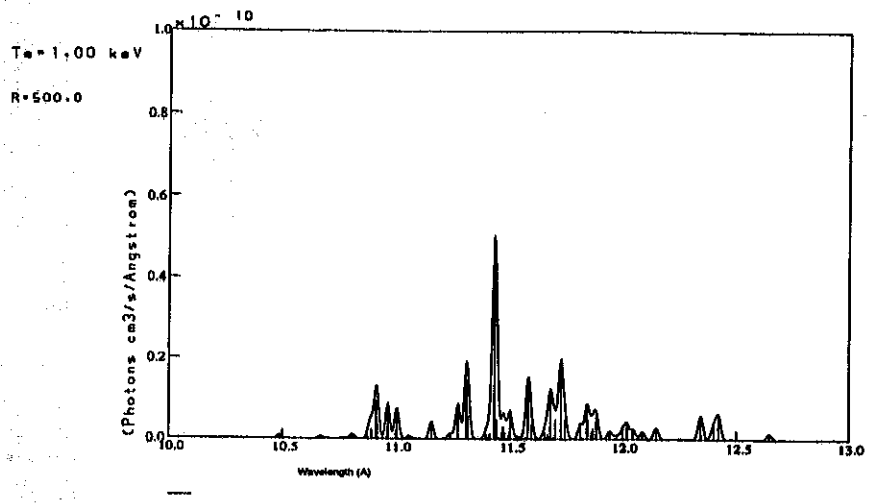

Figure 8: (l) Same as (j) but for recombining plasma component (T_e = 1keV, n_e = 10^{14}cm^{-3}).

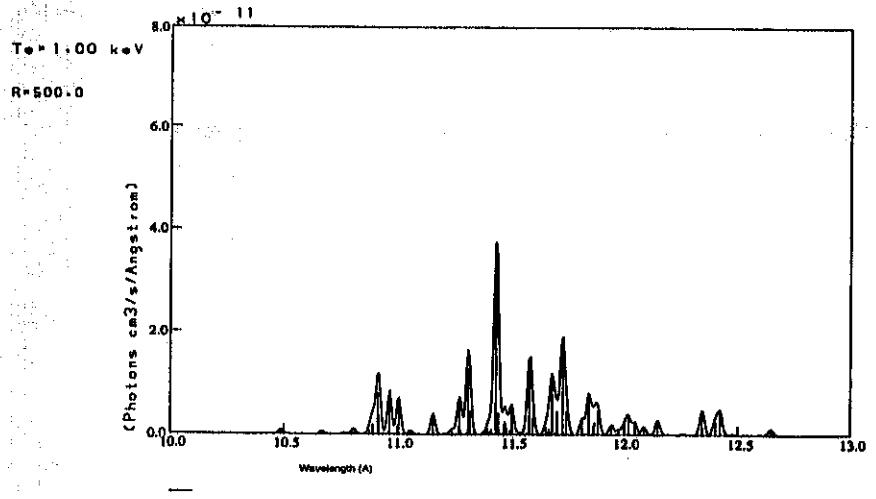

Figure 8: (m) Same as (l) but for n_e = 10^{11}cm^{-3}. (T_e = 1keV; recombining plasma component).

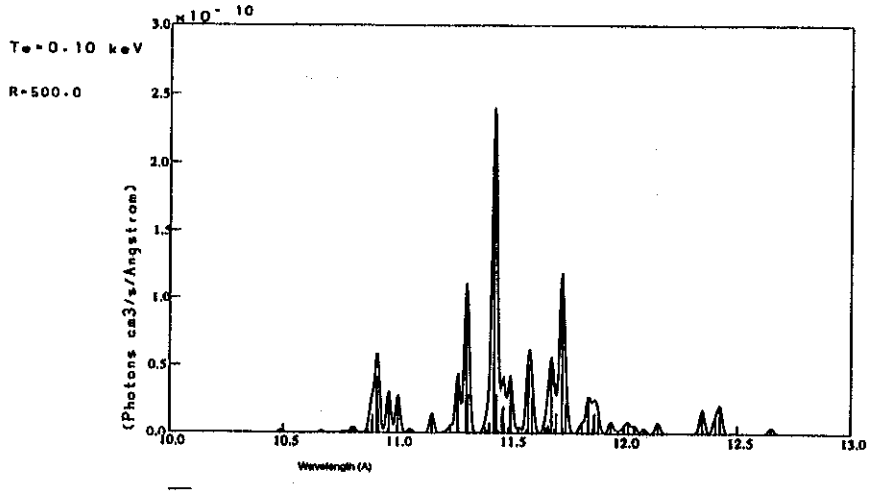

Figure 8: (n) Same as (l) but for T_e = 100eV (n_e = 10^{14}cm^{-3}; recombining plasma component).

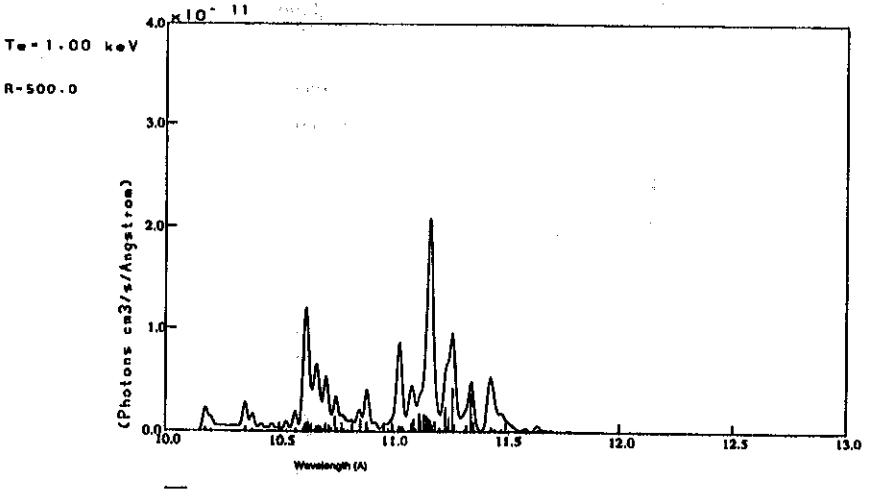

Figure 8: (o) Dielectronic satellite lines for the same plasma as (l) (T_e = 1keV, n_e = 10^{14}cm^{-3}).

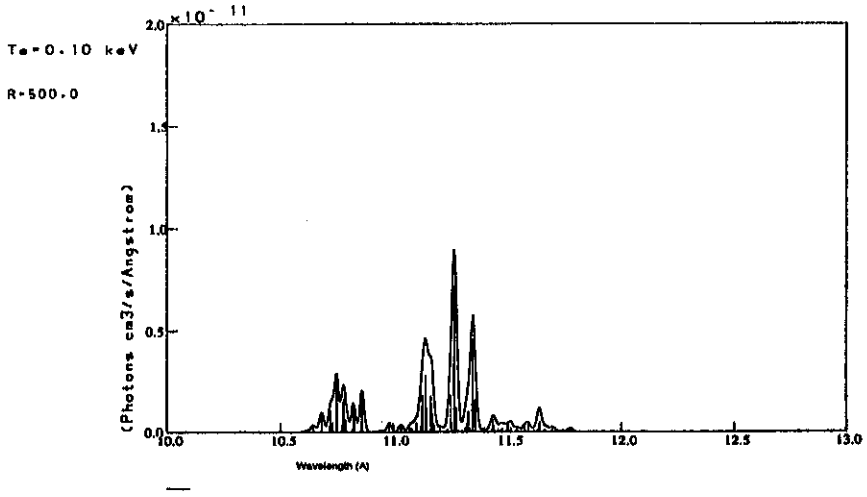

Figure 8: (p) Same as (o) but for $T_e = 100$eV ($n_e = 10^{14}$cm^{-3}).

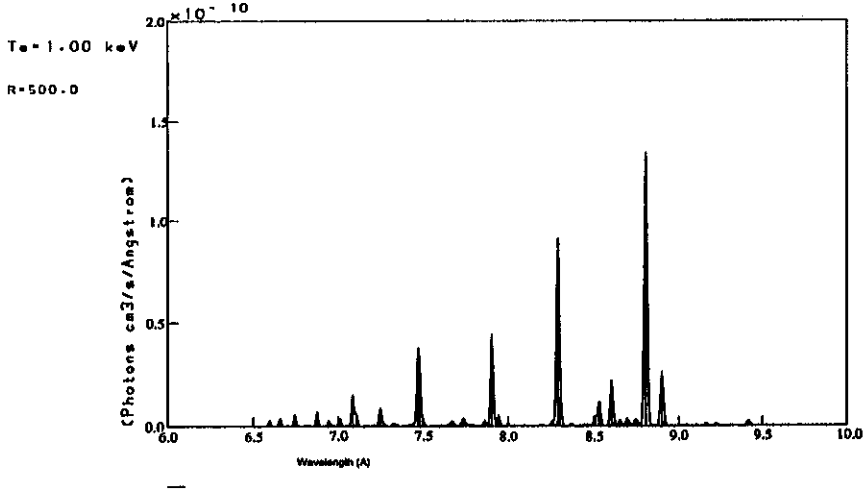

Figure 8: (q) Same as (a) but for $\lambda = 6 - 10$ Å (ionizing plasma component; $T_e = 1$keV, $n_e = 10^{14}$cm^{-3}).

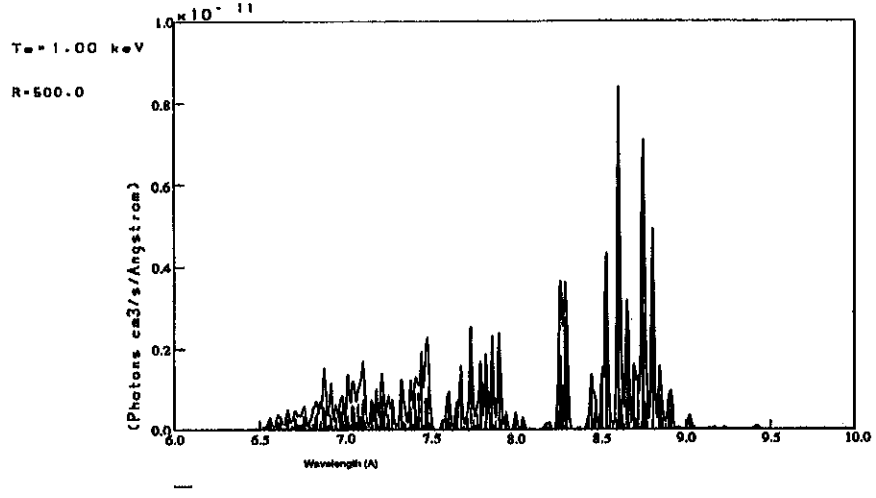

Figure 8: (r) Same as (q) but for recombining plasma component ($T_e = 1$keV, $n_e = 10^{14}$cm^{-3}).

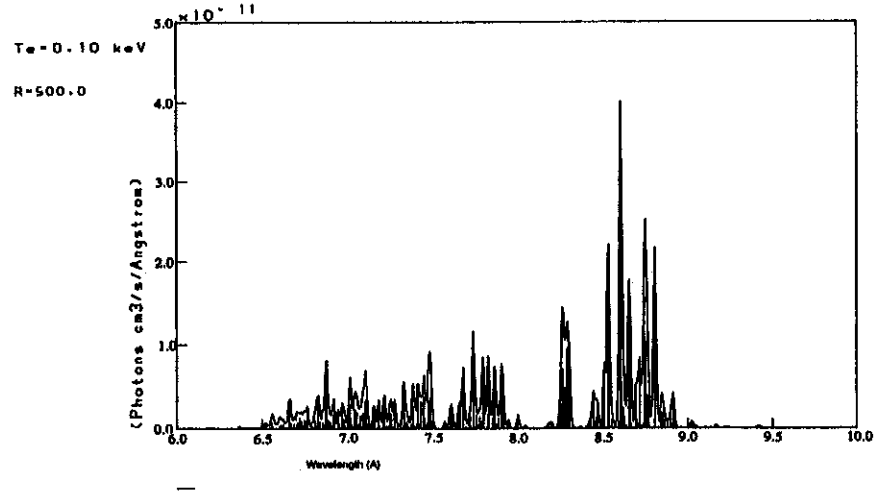

Figure 8: (s) Same as (r) but for $T_e = 100$eV ($n_e = 10^{14}$cm^{-3}; recombining plasma component).

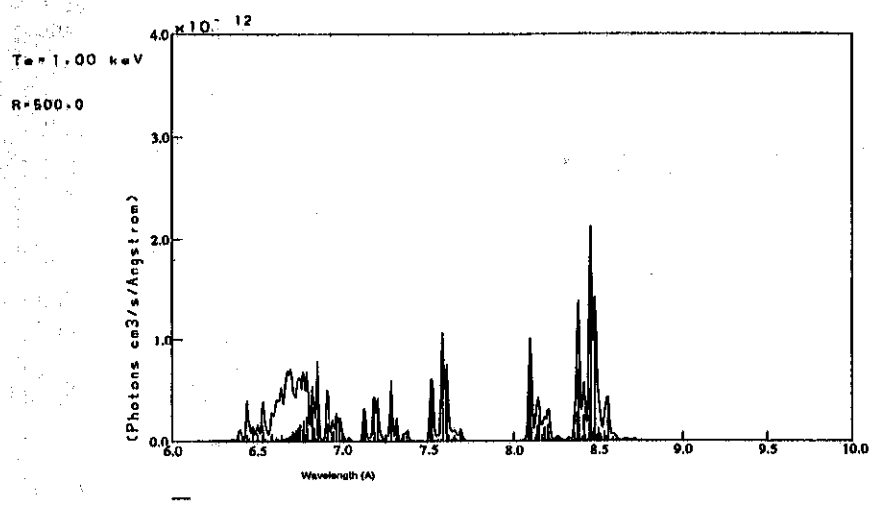

Figure 8: (t) Dielectronic satellite lines for the same plasma as (r) (T_e = 1keV, n_e = 10^{14}cm^{-3}).

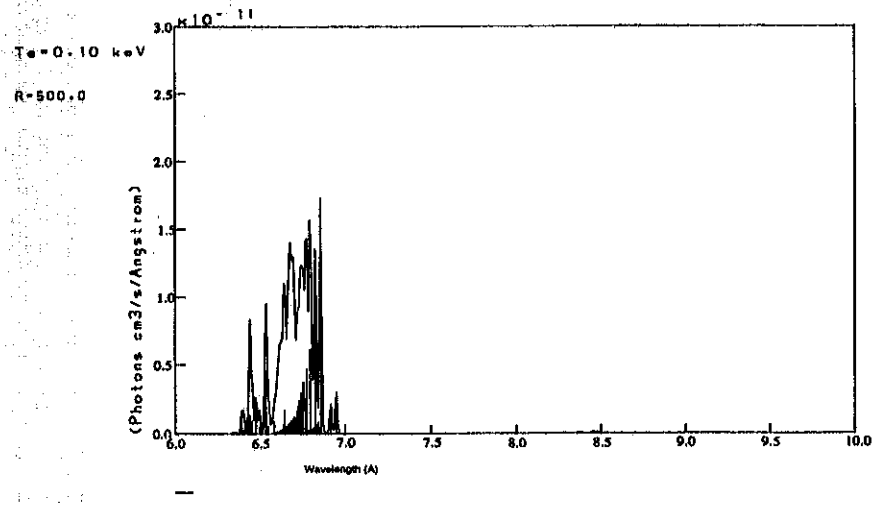

Figure 8: (u) Same as (t) but for T_e = 100eV ($n_e = 10^{14}$cm^{-3}).

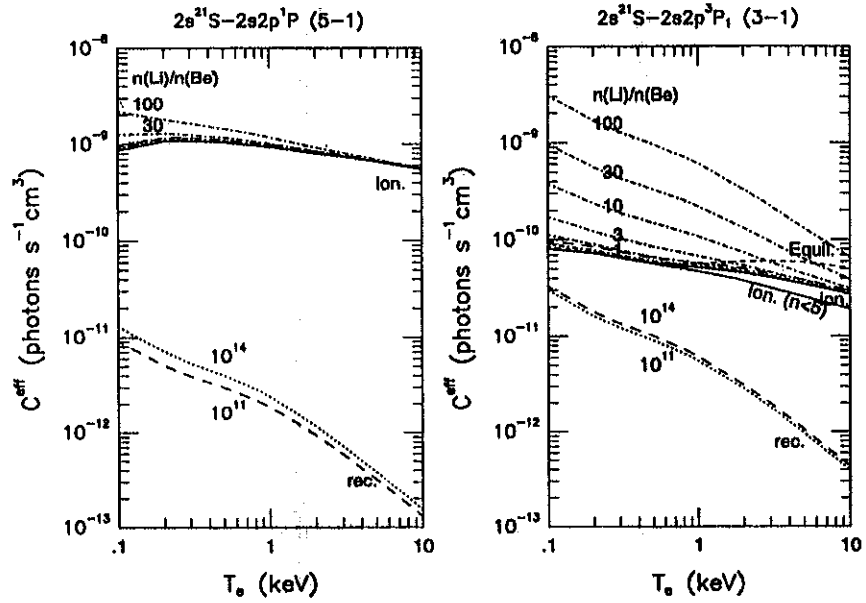

Figure 9: The effective emission rate coefficients as a function of the electron temperature. At $n_e = 10^{14}$cm^{-3} ionizing plasma component (solid line labeled with ion.), recombining plasma component (dotted line labeled with rec.), ionization equilibrium plasma (dashed line labeled with Equil.), and ionization non-equilibrium plasma labeled with assumed ion abundance ration of n(Fe^{23+}) to n(Fe^{22+}) (dot-dashed line) are shown. The ionizing plasma component calculated by CRM with $n \leq 4$ is also shown with solid line labeled with ion.($n < 5$). At $n_e = 10^{11}$cm^{-3} only ionizing plasma component and recombining plasma component (dashed line) are shown. Ion abundance ratio for the ionization equilibrium plasma is taken from Ref.[15] ($T >$ 430eV).

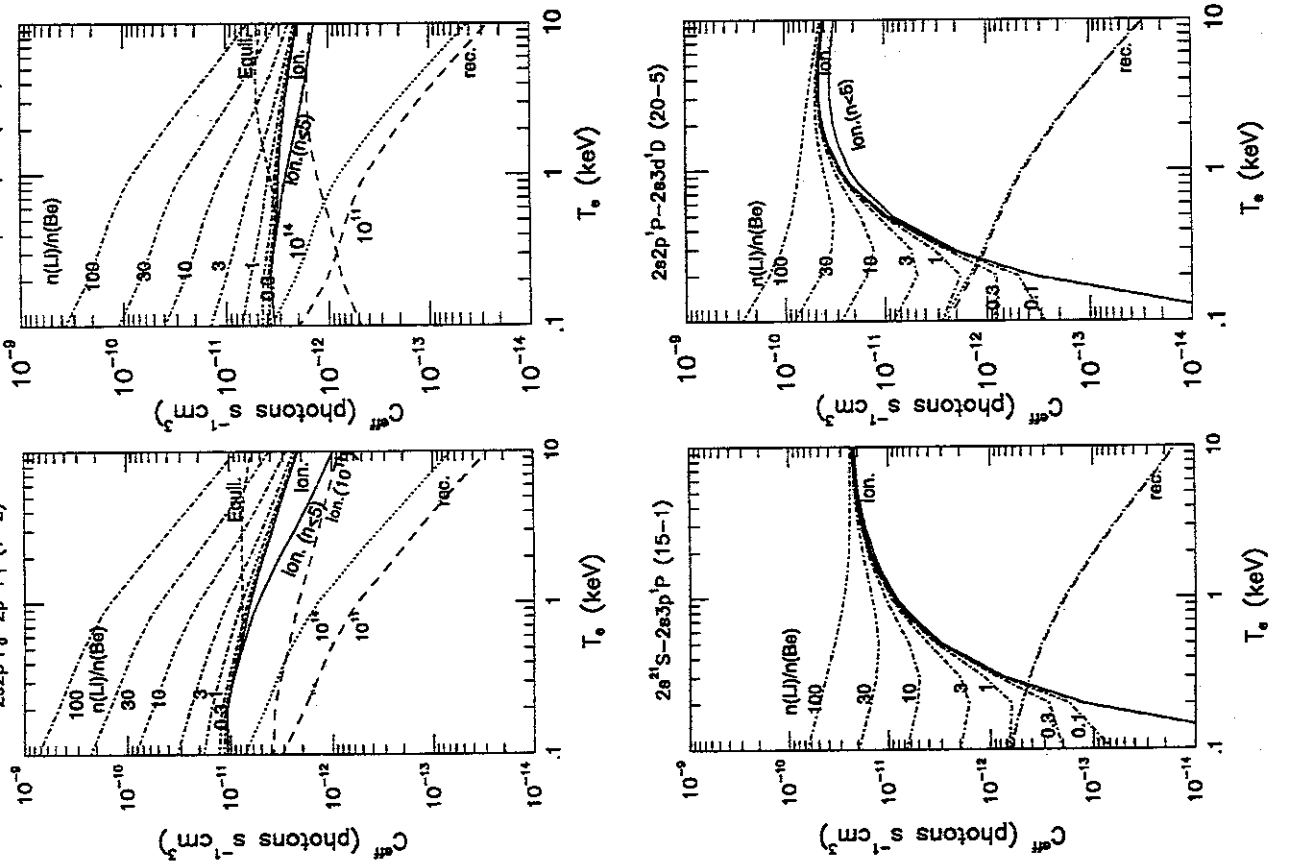

Figure 9: continued.

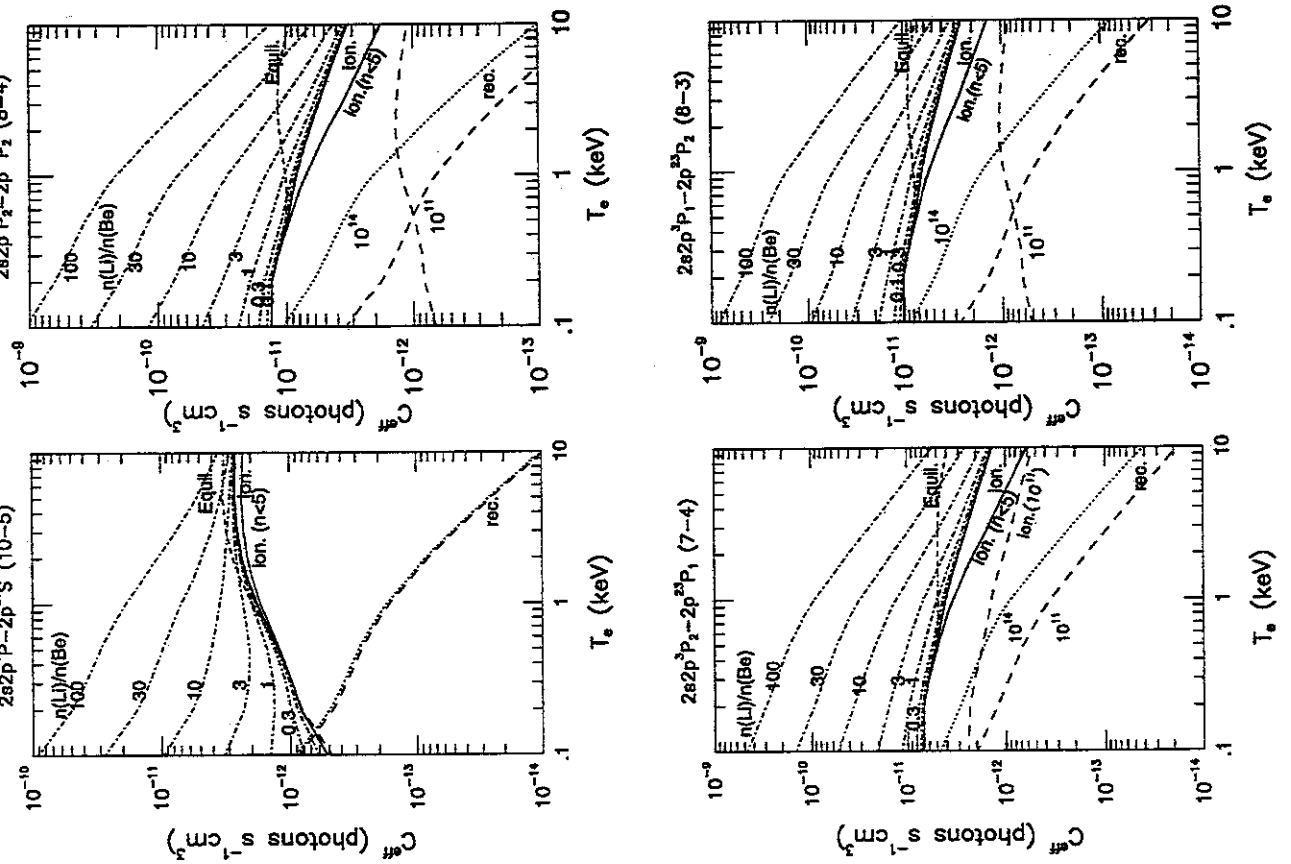

Figure 9: continued.

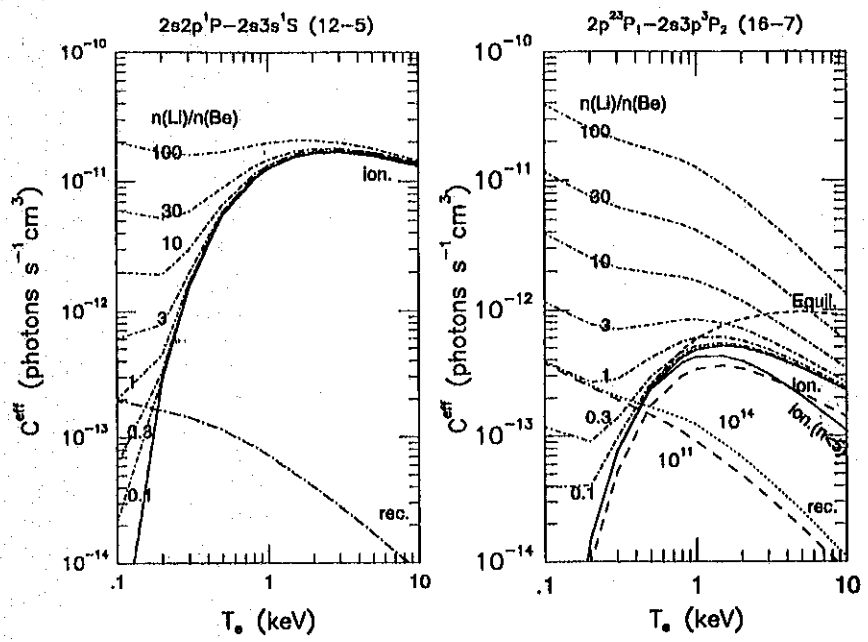

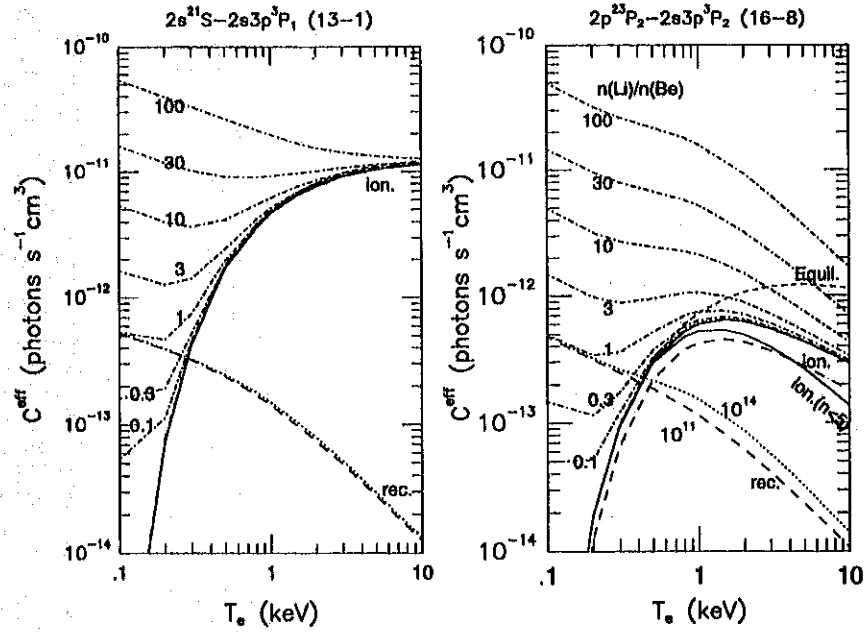

Figure 9: continued.

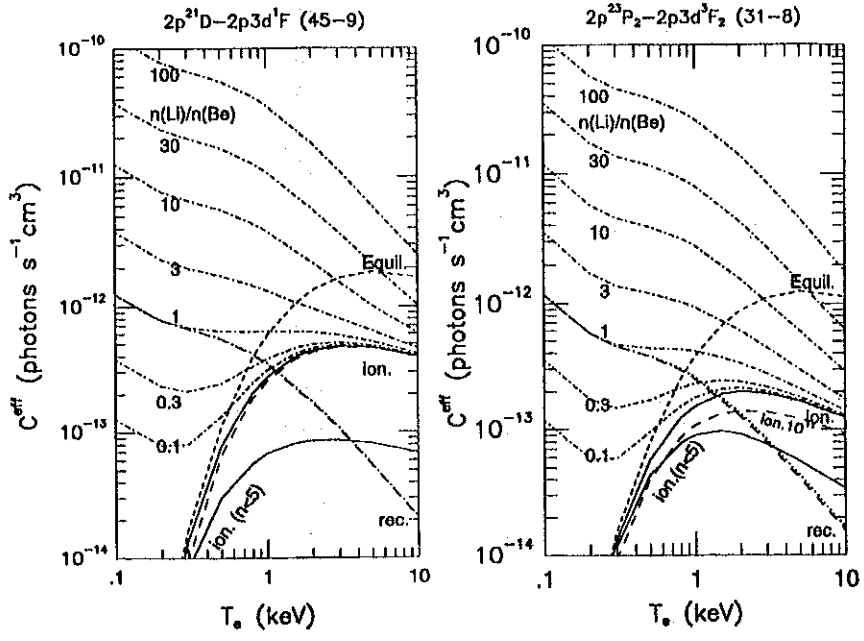

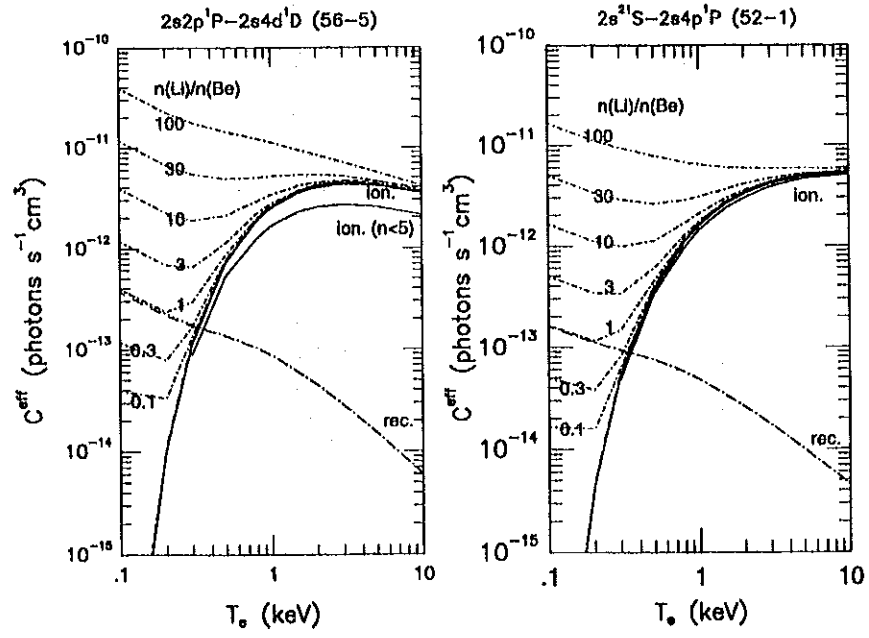

Figure 9: continued.

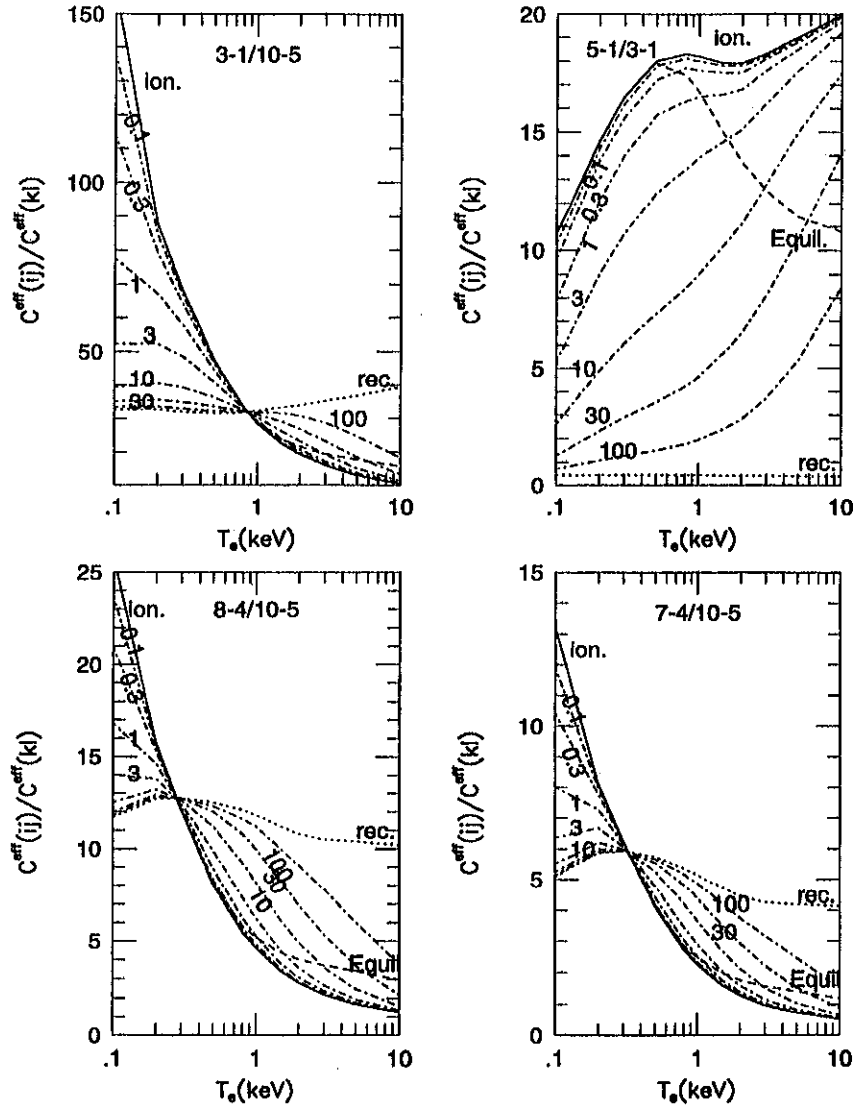

Figure 10: The line intensity ratios as a function of the electron temperature at $n_e = 10^{14}\text{cm}^{-3}$. The cases of the pure ionizing plasma (solid line), the pure recombining plasma (dotted line), the ionization equilibrium plasma (dashed line), and non-equilibrium ionization plasmas with given ion abundance ratios (0.1, 0.3, 1, 3, 10, 30, 100 from the nearest side of ionizing plasma to the nearest side of recombining plasma) with dot-dashed lines are plotted. Ion abundance ratio for the ionization equilibrium plasma is taken from Ref.[15] ($T > 430$eV). Each panel is for different line ratio labeled with the transitions by numbering. Numbering is the same as indicated in Fig.9 and Tables 1-3.

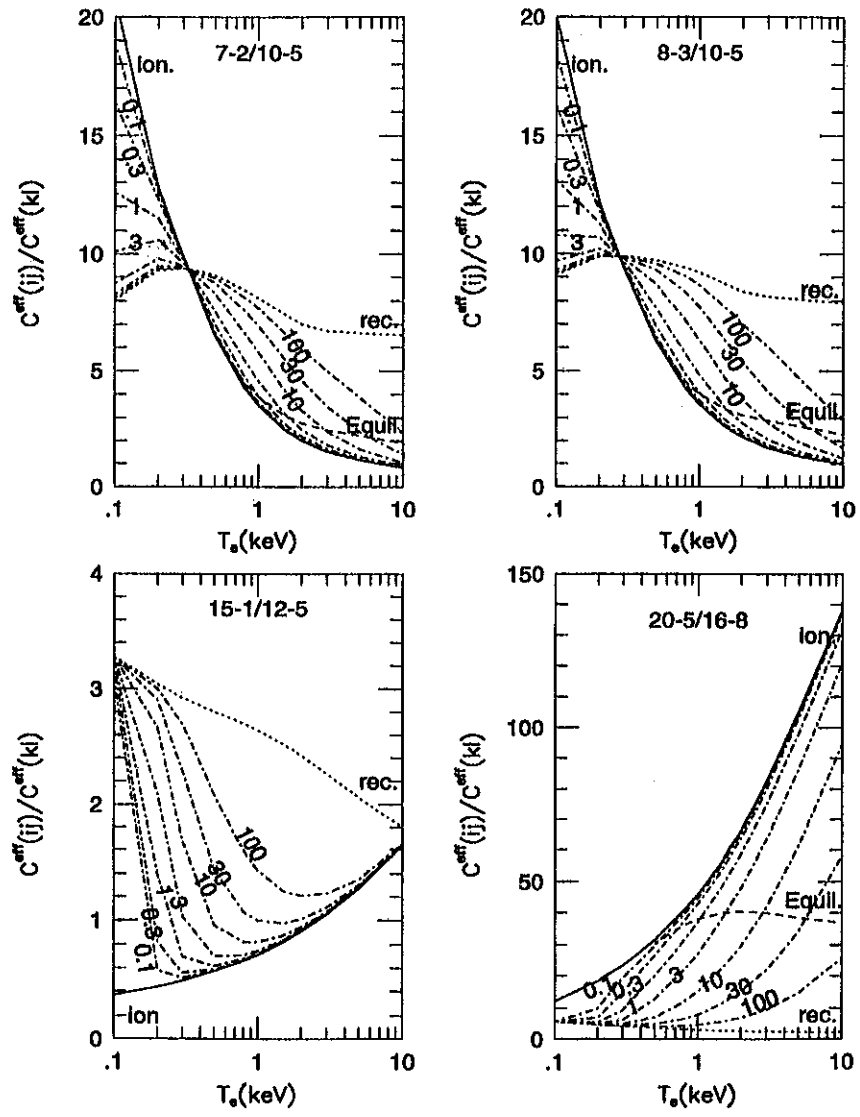

Figure 10: continued. For $n_e = 10^{14}\text{cm}^{-3}$.

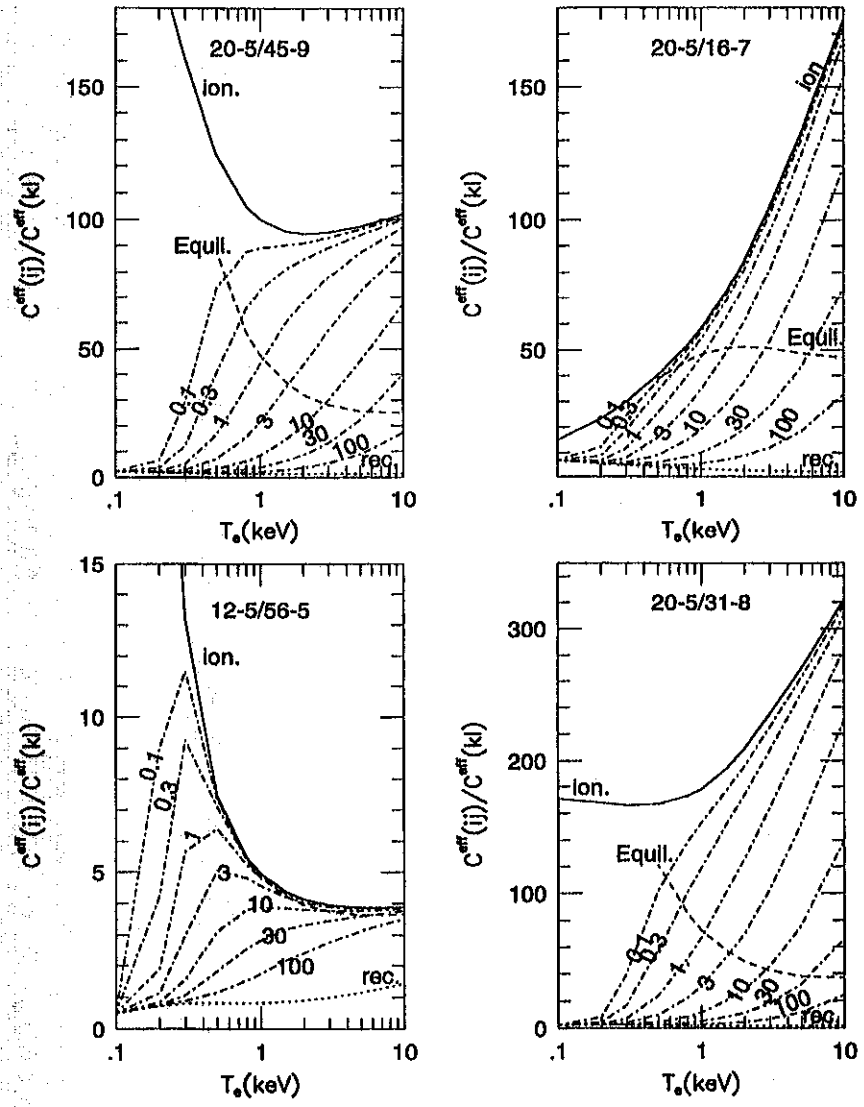

Figure 10: continued. For $n_e = 10^{14}\text{cm}^{-3}$.

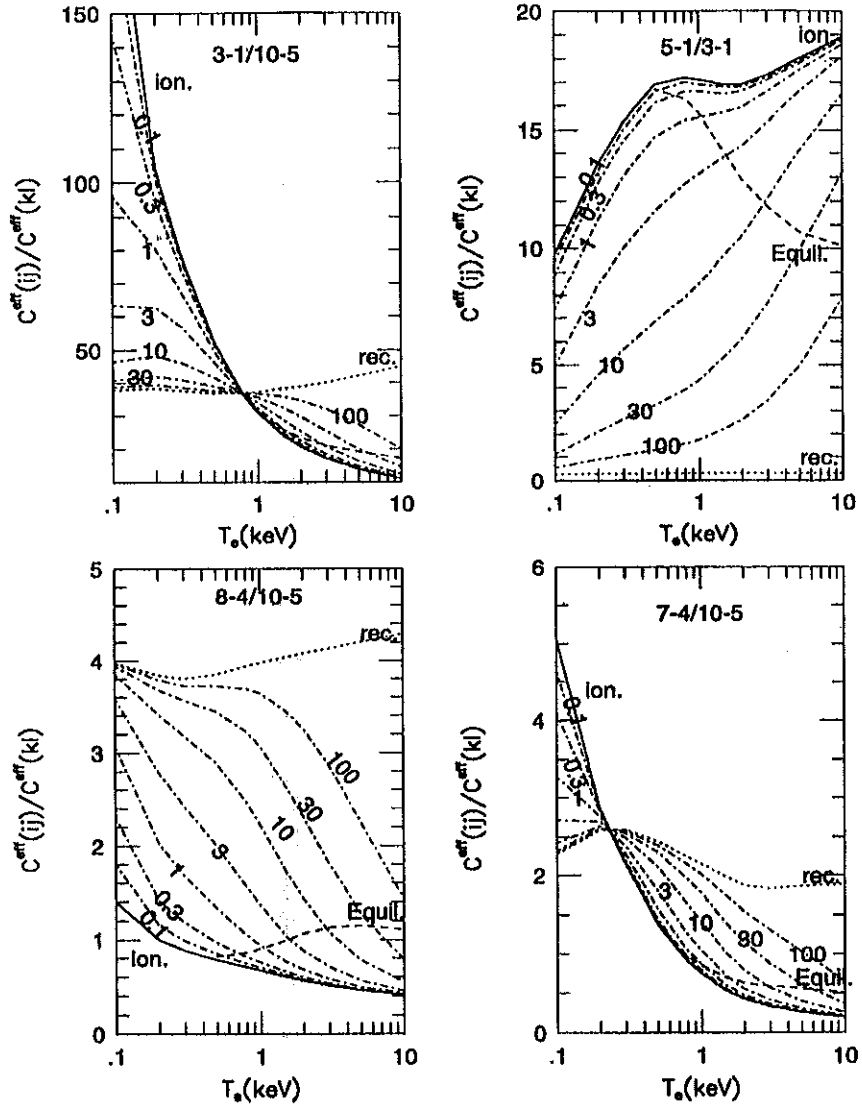

Figure 10: continued. For $n_e = 10^{11}\text{cm}^{-3}$.

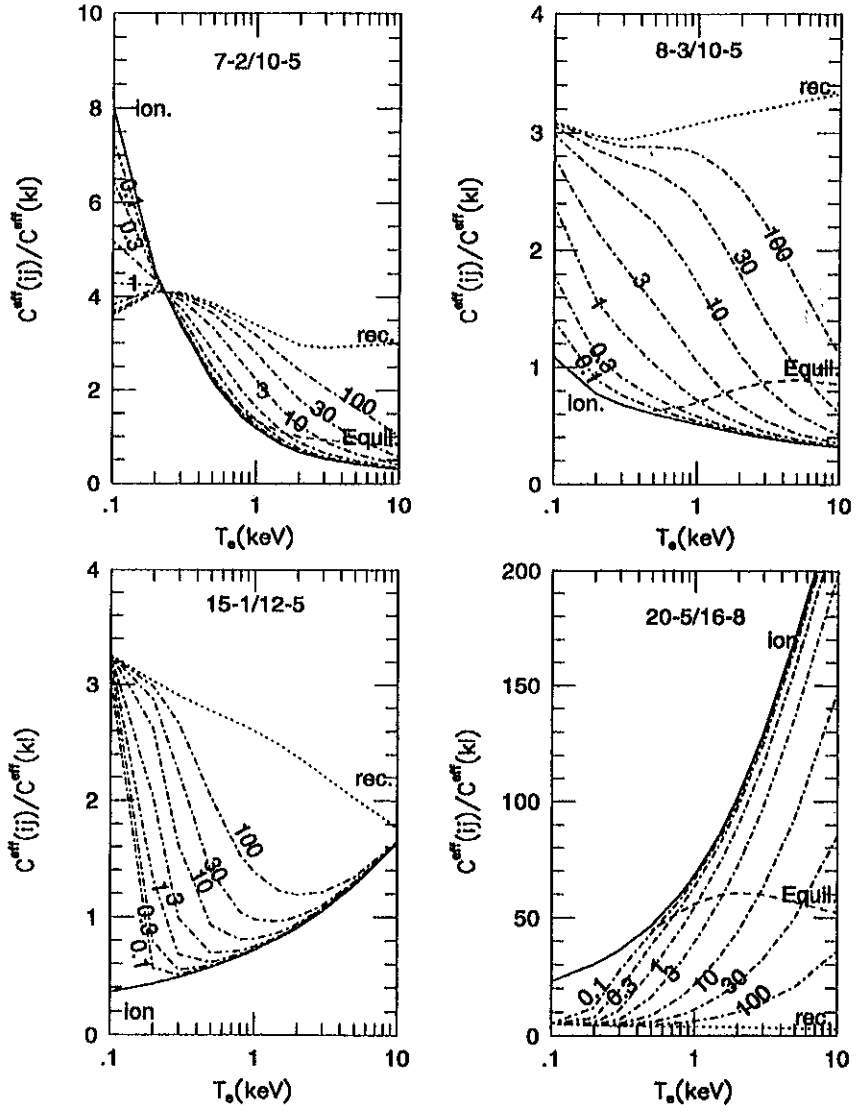

Figure 10: continued. For $n_e = 10^{11}\text{cm}^{-3}$.

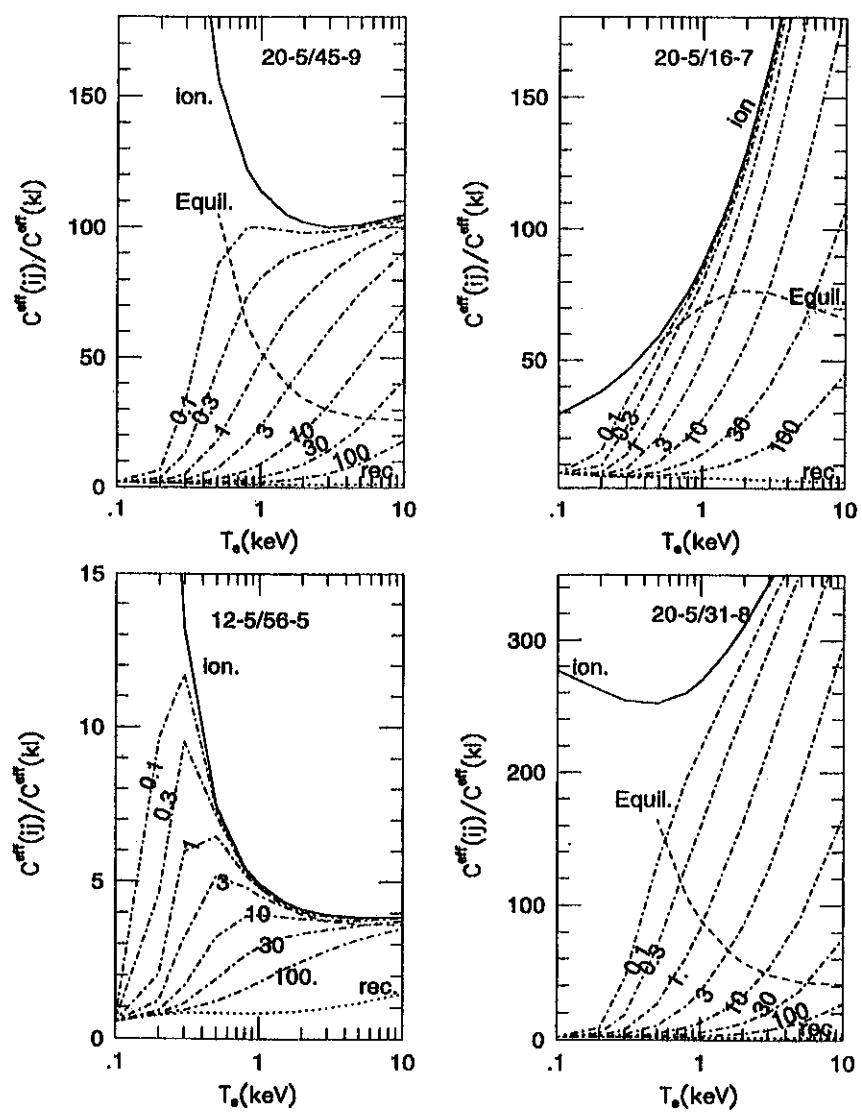

Figure 10: continued. For $n_e = 10^{11}\text{cm}^{-3}$.

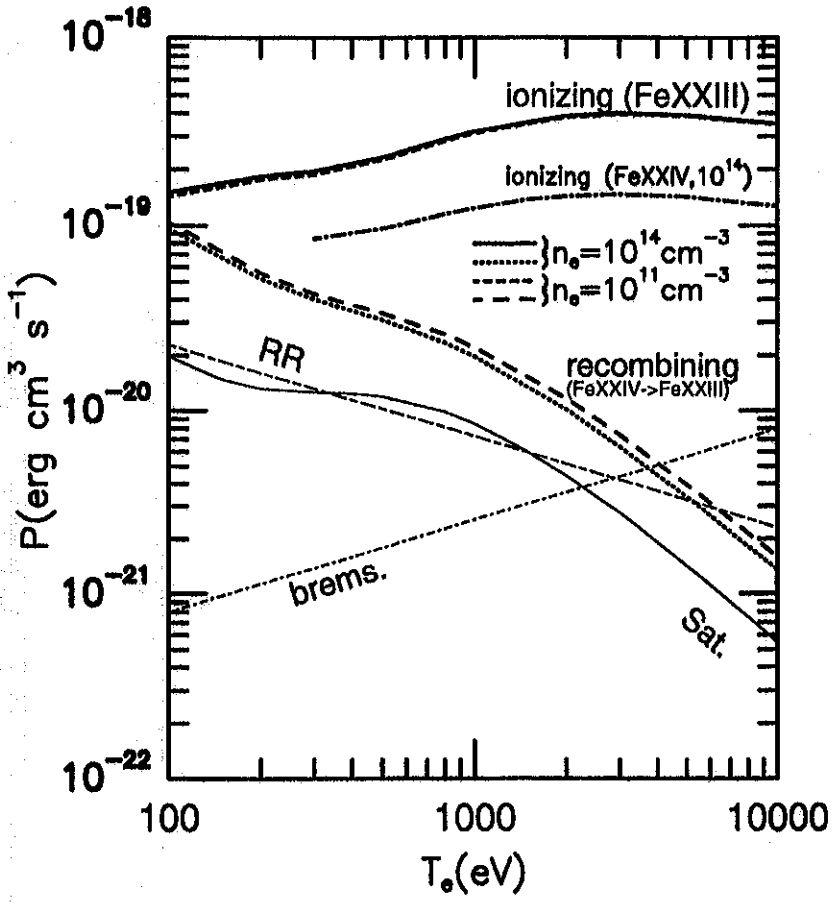

Figure 11: (a) The radiative power losses for ionizing plasma component and recombining plasma component as a function of electron temperature. The radiative power losses due to FeXXIV lines (Fe^{23+} ion), bremsstrahlung, radiative recombination, and satellite lines are also plotted.

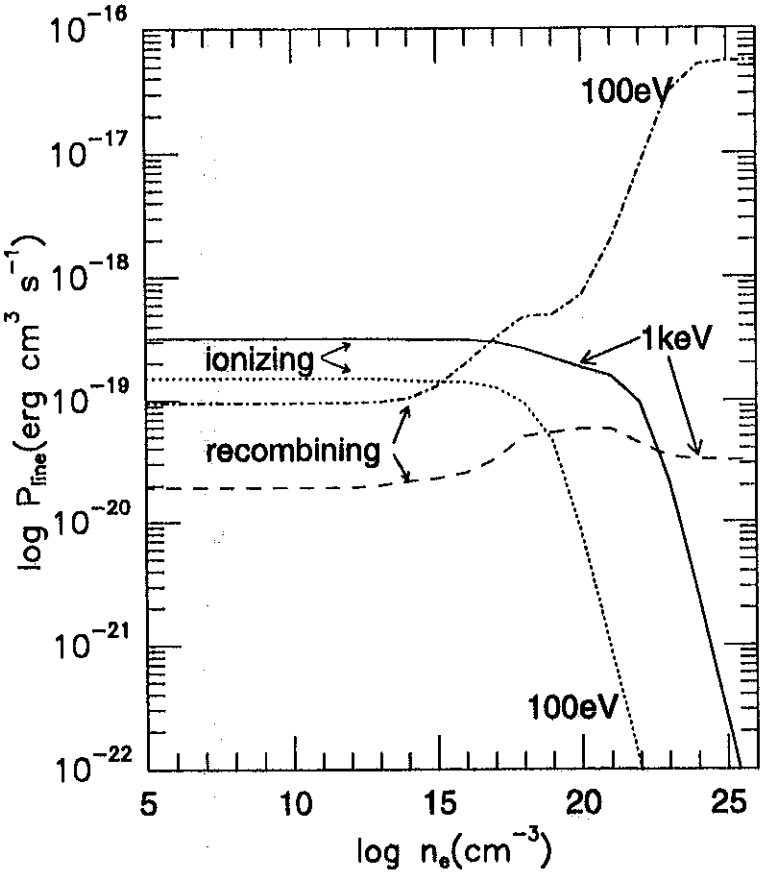

Figure 11: (b) The radiative power losses as a function of electron density.

Publication List of NIFS-DATA Series

NIFS-DATA-1 Y. Yamamura, T. Takiguchi and H. Tawara,
Data Compilation of Angular Distributions of Sputtered Atoms; Jan. 1990

NIFS-DATA-2 T. Kato, J. Lang and K. E. Berrington,
Intensity Ratios of Emission Lines from OV Ions for Temperature and Density Diagnostics ; Mar. 1990 [At Data and Nucl Data Tables 44(1990)133]

NIFS-DATA-3 T. Kaneko,
Partial Electronic Straggling Cross Sections of Atoms for Protons; Mar. 1990

NIFS-DATA-4 T. Fujimoto, K. Sawada and K. Takahata,
Cross Section for Production of Excited Hydrogen Atoms Following Dissociative Excitation of Molecular Hydrogen by Electron Impact ; Mar. 1990

NIFS-DATA-5 H. Tawara,
Some Electron Detachment Data for H^- Ions in Collisions with Electrons, Ions, Atoms and Molecules – an Alternative Approach to High Energy Neutral Beam Production for Plasma Heating–;Apr. 1990

NIFS-DATA-6 H. Tawara, Y. Itikawa, H. Nishimura, H. Tanaka and Y. Nakamura,
Collision Data Involving Hydro-Carbon Molecules ; July 1990 [Supplement to Nucl. Fusion 2(1992)25]

NIFS-DATA-7 H.Tawara,
Bibliography on Electron Transfer Processes in Ion-Ion/Atom/Molecule Collisions –Updated 1990–; Aug. 1990

NIFS-DATA-8 U.I.Safronova, T.Kato, K.Masai, L.A.Vainshtein and A.S.Shlyapzeva,
Excitation Collision Strengths, Cross Sections and Rate Coefficients for OV, SiXI, FeXXIII, MoXXXIX by Electron Impact ($1s^22s^2$-$1s^22s2p$-$1s^22p^2$ Transitions) Dec.1990

NIFS-DATA-9 T.Kaneko,
Partial and Total Electronic Stopping Cross Sections of Atoms and Solids for Protons; Dec. 1990

NIFS-DATA-10 K.Shima, N.Kuno, M.Yamanouchi and H.Tawara,
Equilibrium Charge Fraction of Ions of Z=4-92 (0.02-6 MeV/u) and Z=4-20 (Up to 40 MeV/u) Emerging from a Carbon Foil; Jan.1991 [AT.Data and Nucl. Data Tables 51(1992)173]

NIFS-DATA-11 T. Kaneko, T. Nishihara, T. Taguchi, K. Nakagawa, M. Murakami, M. Hosono, S. Matsushita, K. Hayase, M.Moriya, Y.Matsukuma, K.Miura and Hiro Tawara,
Partial and Total Electronic StoppingCross Sections of Atoms for a Singly Charged Helium Ion: Part I; Mar. 1991

NIFS-DATA-12 Hiro Tawara,
Total and Partial Cross Sections of Electron Transfer Processes for Be^{q+} and B^{q+} Ions in Collisions with H, H_2 and He Gas Targets -Status in 1991-; June 1991

NIFS-DATA-13 T. Kaneko, M. Nishikori, N. Yamato, T. Fukushima, T. Fujikawa, S. Fujita, K. Miki, Y. Mitsunobu, K. Yasuhara, H. Yoshida and Hiro Tawara,
Partial and Total Electronic Stopping Cross Sections of Atoms for a Singly Charged Helium Ion : Part II; Aug. 1991

NIFS-DATA-14 T. Kato, K. Masai and M. Arnaud,
Comparison of Ionization Rate Coefficients of Ions from Hydrogen through Nickel ; Sep. 1991

NIFS-DATA-15 T. Kato, Y. Itikawa and K. Sakimoto,
Compilation of Excitation Cross Sections for He Atoms by Electron Impact; Mar. 1992

NIFS-DATA-16 T. Fujimoto, F. Koike, K. Sakimoto, R. Okasaka, K. Kawasaki, K. Takiyama, T. Oda and T. Kato,
Atomic Processes Relevant to Polarization Plasma Spectroscopy ; Apr. 1992

NIFS-DATA-17 H. Tawara,
Electron Stripping Cross Sections for Light Impurity Ions in Colliding with Atomic Hydrogens Relevant to Fusion Research; Apr. 1992

NIFS-DATA-18 T. Kato,
Electron Impact Excitation Cross Sections and Effective Collision Strengths of N Atom and N-Like Ions -A Review of Available Data and Recommendations- ; Sep. 1992

NIFS-DATA-19 Hiro Tawara,
Atomic and Molecular Data for H_2O, CO & CO_2 Relevant to Edge Plasma Impurities, Oct. 1992

NIFS-DATA-20 Hiro. Tawara,
Bibliography on Electron Transfer Processes in Ion-Ion/Atom/Molecule Collisions -Updated 1993-; Apr. 1993

NIFS-DATA-21 J. Dubau and T. Kato,
Dielectronic Recombination Rate Coefficients to the Excited States of C I from C II; Aug. 1994

NIFS-DATA-22 T. Kawamura, T. Ono, Y. Yamamura,
Simulation Calculations of Physical Sputtering and Reflection Coefficient of Plasma-Irradiated Carbon Surface; Aug. 1994

NIFS-DATA-23 Y. Yamamura and H. Tawara,
Energy Dependence of Ion-Induced Sputtering Yields from Monoatomic Solids at Normal Incidence; Mar. 1995

NIFS-DATA-24 T. Kato, U. Safronova, A. Shlyaptseva, M. Cornille, J. Dubau,
Comparison of the Satellite Lines of H-like and He-like Spectra; Apr. 1995

NIFS-DATA-25 H. Tawara,
Roles of Atomic and Molecular Processes in Fusion Plasma Researches - from the cradle (plasma production) to the grave (after-burning) -; May 1995

NIFS-DATA-26 N. Toshima and H. Tawara
Excitation, Ionization, and Electron Capture Cross Sections of Atomic Hydrogen in Collisions with Multiply Charged Ions; July 1995

NIFS-DATA-27 V.P. Shevelko, H. Tawara and E.Salzborn,
Multiple-Ionization Cross Sections of Atoms and Positive Ions by Electron Impact; July 1995

NIFS-DATA-28 V.P. Shevelko and H. Tawara,
Cross Sections for Electron-Impact Induced Transitions Between Excited States in He: n, n'=2,3 and 4; Aug. 1995

NIFS-DATA-29 U.I. Safronova, M.S. Safronova and T. Kato,
Cross Sections and Rate Coefficients for Excitation of $\Delta n = 1$ Transitions in Li-like Ions with $6<Z<42$; Sep. 1995

NIFS-DATA-30 T. Nishikawa, T. Kawachi, K. Nishihara and T. Fujimoto,
Recommended Atomic Data for Collisional-Radiative Model of Li-like Ions and Gain Calculation for Li-like Al Ions in the Recombining Plasma; Sep. 1995

NIFS-DATA-31 Y. Yamamura, K. Sakaoka and H. Tawara,
Computer Simulation and Data Compilation of Sputtering Yield by Hydrogen Isotopes ($^1H^+$, $^2D^+$, $^3T^+$) and Helium ($^4He^+$) Ion Impact from Monatomic Solids at Normal Incidence; Oct. 1995

NIFS-DATA-32 T. Kato, U. Safronova and M. Ohira,
Dielectronic Recombination Rate Coefficients to the Excited States of CII from CIII; Feb. 1996

NIFS-DATA-33 K.J. Snowdon and H. Tawara,
Low Energy Molecule-Surface Interaction Processes of Relevance to Next-Generation Fusion Devices; Mar. 1996

NIFS-DATA-34 T. Ono, T. Kawamura, K. Ishii and Y. Yamamura,
Sputtering Yield Formula for B_4C Irradiated with Monoenergetic Ions at Normal Incidence; Apr. 1996

NIFS-DATA-35 I. Murakami, T. Kato and J. Dubau,

UV and X-Ray Spectral Lines of Be-Like Fe Ion for Plasma Diagnostics; Apr. 1996

NIFS-DATA-36 K. Moribayashi and T. Kato,
Dielectronic Recombination of Be-like Fe Ion; Apr. 1996

NIFS-DATA-37 U. Safronova, T. Kato and M. Ohira,
Dielectronic Recombination Rate Coefficients to the Excited States of CIII from CIV; July 1996

NIFS-DATA-38 T. Fujimoto, H. Sahara, G. Csanak and S. Grabbe,
Atomic States and Collisional Relaxation in Plasma Polarization Spectroscopy: Axially Symmetric Case; Oct. 1996

NIFS-DATA-39 H. Tawara (Ed.)
Present Status on Atomic and Molecular Data Relevant to Fusion Plasma Diagnostics and Modeling; Jan. 1997

NIFS-DATA-40 Inga Yu. Tolstikhina,
LS-Averaged 1/Z Method as a Tool of Studying the Interactions of Highly Charged Ions with a Metal Surface; Jan. 1997

NIFS-DATA-41 K. Moribayashi and T. Kato,
Atomic Nuclear Charge Scaling for Dielectronic Recombination to Be-like Ions; Apr. 1997

NIFS-DATA-42 H. Tawara,
Bibliography on Electron Transfer Processes in Ion-ion / Atom / Molecule Collisions -Updated 1997 -; May 1997

NIFS-DATA-43 M. Goto and T. Fujimoto,
Collisional-radiative Model for Neutral Helium in Plasma: Excitation Cross Section and Singlet-triplet Wavefunction Mixing; Oct. 1997

NIFS-DATA-44 J. Dubau, T. Kato and U.I. Safronova,
Dielectronic Recombination Rate Coefficients to the Excited States of CI From CII; Jan. 1998

NIFS-DATA-45 Y. Yamamura, W. Takeuchi and T. Kawamura,
The Screening Length of Interatomic Potential in Atomic Collisions; Mar. 1998

NIFS-DATA-46 T. Kenmotsu, T. Kawamura, T. Ono and Y. Yamamura,
Dynamical Simulation for Sputtering of B4C; Mar. 1998

NIFS-DATA-47 I. Murakami, K. Moribayashi and T. Kato,
Effect of Recombination Processes on FeXXIII Line Intensities; May 1998